The First Post-injection Seismic Monitor Survey at the Ketzin Pilot CO₂ Storage Site: Results from Time-lapse Analysis

Fei Huang[1][*], Peter Bergmann[2,3], Christopher Juhlin[1], Monika Ivandic[1], Stefan Lüth[2], Alexandra Ivanova[2], Thomas Kempka[2], Jan Henninges[2], Daniel Sopher[1] and Fengjiao Zhang[4,1]

[1] Department of Earth Sciences, Uppsala University, Villavägen 16, Uppsala 75236, Sweden
[2] GFZ German Research Centre for Geosciences, Telegrafenberg, 14473 Potsdam, Germany
[3] Sintef Petroleum Research, S.P. Andersens vei 15 B, NO-7031 Trondheim, Norway
[4] Jilin University, Xi Min Zhu Street No. 938, Changchun, China

* Corresponding author. Tel.: +46 18 471 3322; fax: +46 18 501 110.
E-mail address: fei.huang@geo.uu.se (F. Huang)

ABSTRACT

The injection of CO₂ at the Ketzin pilot CO₂ storage site started in June 2008 and ended in August 2013. During the 62 months of injection, a total amount of about 67 kt of CO₂ was injected into a saline aquifer. A third repeat 3D seismic survey, serving as the first post-injection survey was acquired in 2015, aiming to investigate the recent movement of the injected CO₂. Consistent with the previous two time-lapse surveys, a predominantly WNW migration of the gaseous CO₂ plume in the up-dip direction within the reservoir is inferred in this first post-injection survey. No systematic anomalies are detected through the reservoir overburden. The extent of the CO₂ plume west of the injection site is almost identical to that found in the 2012 second repeat survey (after injection of 61 kt), however there is a significant decrease in its size east of the injection site. Assessment of the CO₂ plume distribution suggests that the decrease in the size of the anomaly may be due to multiple factors, such as limited vertical resolution, CO₂ dissolution and CO₂ diffusion, in addition to the effects of ambient noise. 4D seismic modelling based on dynamic flow simulations indicates that a dynamic balance between the newly injected CO₂ after the second repeat survey and the CO₂ being dissolved and diffused was reached by the time of the first post-injection survey. Considering the considerable uncertainties in CO₂ mass estimation, both patchy and non-patchy saturation models for the Ketzin site were taken into consideration.

1. INTRODUCTION

Carbon capture and storage (CCS) is one of the potential approaches to reduce CO_2 emissions to the atmosphere on a significant scale. It is set to play an increasingly important role in reducing global CO_2 emissions given that fossil fuels will continue to be utilized significantly in the foreseeable future (Stocker *et al.* 2013). Several large-scale CCS projects in the world, such as the Snøhvit project in the Barents Sea (Hansen *et al.* 2013) and the In Salah project in Algeria (Ringrose *et al.* 2013), provide confidence and operational field experience in CO_2 geologic storage. In April 2004 at the Ketzin pilot site, west of Berlin (Fig. 1), the CO_2SINK project (Förster *et al.* 2006) financed by the European Commission was launched as the first onshore pilot scale CO_2 storage experiment in Europe. It had the aim of verifying CO_2 monitoring methods and understanding CO_2 geologic storage in a saline aquifer. The borehole Ktzi 201, serving as the injection well, together with two observation wells, Ktzi 200 and Ktzi 202, were drilled down to a depth of approximately 800 m in 2007. In the summer of 2011, a shallow observation well, P300, was drilled to the lowermost sandstone above the caprock for the purpose of monitoring storage integrity (Martens *et al.* 2012). In August and September 2012, after more than four years of a CO_2 injection, another observation well, Ktzi 203, was drilled to the same depth level as the wells drilled in 2007 (Prevedel *et al.* 2014). Between June 2008 and August 2013, about 67 kt of CO_2 were injected into the sandstone units at the depth of 630–650 m through the injection well Ktzi 201.

The replacement of the reservoir brine by CO_2 leads to a decrease in the P-wave velocity and density of the reservoir rock, and consequently an increase in the impedance contrast to higher velocity caprock. These changes in the reservoir can be imaged by seismic techniques. A broad range of

seismic methods have been implemented at the Ketzin site to image the subsurface structure and the distribution of the CO_2 plume. The near-surface structure was mapped using first arrivals obtained from a 2D surface seismic pilot survey (Yordkayhun *et al.* 2007). Reflections from moving source profiling data acquired in 2007 show detailed information of the sandstone reservoir around the borehole zone (Yang *et al.* 2010). The application of waveform tomography on time-lapse cross-well seismic surveys conducted between May 2008 and July 2009 presents the feasibility of monitoring velocity changes due to CO_2 injection (Zhang *et al.* 2012). The results of passive seismic surveys show the potential for reconstruction of subsurface structure from ambient noise (Xu *et al.* 2012). 2D time-lapse measurements were carried out for imaging the subsurface structure and monitoring the CO_2 movement (Bergmann *et al.* 2011). Three sparse 3D seismic measurements (seven 2D lines forming a star-shaped geometry) were implemented to build a link between downhole surveys and conventional 3D surface seismic surveys (Ivandic *et al.* 2012). In comparison with the other seismic surveys, 3D seismic surveys can provide comprehensive coverage of the subsurface and better lateral resolution. Between autumn 2005 and autumn 2015 four full 3D seismic surveys were performed at the Ketzin site. These include one baseline survey before CO_2 injection and three repeat surveys after CO_2 injection started. Results from the 3D seismic time-lapse analysis prove the effectiveness of the approach in monitoring the movement of the injected CO_2 at the Ketzin pilot site.

CO_2 injection ceased in August 2013 and the Ketzin pilot site entered the post-closure phase (Martens *et al.* 2014). In order to investigate the latest movement of the injected CO_2, the third repeat survey, serving as the first post-injection survey, was acquired in autumn 2015, two years after the end of the injection. In this study, we present the processing results obtained from the first post-injection survey and utilize the time-lapse analysis to study the CO_2 behavior. Quantitative analysis using both patchy and non-patchy saturation models is performed to estimate the mass of

the imaged CO_2. Time-lapse results show considerable post-injection changes in the CO_2 plume behavior at the Ketzin pilot site.

2. Geologic setting

The Ketzin anticline is a part of a double anticline, resulting from the movement related to an elongated salt pillow at 1500-2000 m depth (Förster *et al.* 2006). The CO_2 storage site is situated on the southern flank of the Ketzin anticline with a dip angle of around 15 degrees. The target formation for CO_2 storage is the 75-80 m thick Triassic Stuttgart Formation. The Stuttgart Formation is very lithologically heterogeneous, containing both muddy, flood-plain-facies (poor reservoir quality) and sandy channel-facies (good reservoir quality). According to well-log analysis, variable permeability in a range of 0.02 to 5000 md and porosity in a range of 5 to 35% are found within the Stuttgart Formation (Norden *et al.* 2010). The upper part of the Stuttgart Formation contains a 9-20 m thick main-reservoir sandstone unit. The measured reservoir pressure and temperature ranges from 6.21 to 6.47 MPa (Kazemeini 2009) and from 34 to 38 $^{\circ}$C (Förster *et al.* 2006), respectively. The overlying formation of the reservoir is the Weser Formation composed mainly of mudstone and anhydrite. The top part of the Weser Formation contains a 10-20 m thick anhydrite layer located approximately 80 m above the top of the Stuttgart Formation. This anhydrite layer exhibits good sealing characteristics and generates a strong seismic reflection named the K2 reflector in vintage seismic data (Juhlin *et al.* 2007). Above the Weser Formation is the Arnstadt Formation which consists mainly of mudstone and carbonates. These two formations are defined as the caprocks above the reservoir due to their low permeability (Norden *et al.* 2010). Above these caprocks, Jurassic sandstones, in which natural gas was stored between the 1970s and 2000, are found in conjunction with anhydrite, siltstone and mudstone interlayers, constituting a multi-aquifer system. An 80-90 m thick Tertiary clay serving as the caprock for this aquifer system isolates the saline waters in the aquifers from the overlying fresh water within the Quaternary section.

3. OVERVIEW OF 3D SEISMIC ACTIVITIES AT THE KETZIN SITE

The first 3D seismic survey, acting as the baseline for the subsequent 3D surveys was acquired in 2005, prior to CO_2 injection and covers an area of around 12 km^2 (Juhlin *et al.* 2007). Two 3D repeat surveys were acquired in the autumns of 2009 and 2012, after the injection of about 22 and 61 kt of CO_2, respectively (Ivanova *et al.* 2012; Ivandic *et al.* 2015). Figure 1 shows the template schemes employed in the previous 3D surveys. The same acquisition geometry was used within each template (Juhlin *et al.* 2007). A total of 41 templates were acquired in the baseline survey while 20 and 31 templates were recorded in the first and second repeat surveys, respectively. Almost identical processing steps (except for static corrections which are affected by weather and ground conditions) were used for the baseline and two repeat surveys in order to improve the repeatability in the time-lapse data.

Figure 2 shows the contour lines at the 0.3 level extracted from the normalized amplitude difference horizons at the reservoir top level for the first repeat and second repeat surveys (Ivanova *et al.* 2012; Ivandic *et al.* 2015). It has been assumed that these contour lines at 0.3 define the extent of the gaseous CO_2 plume that can be imaged for each survey reasonably well since values smaller than 0.25 are widespread over the entire survey area, and therefore are regarded as non-repeatable noise (Ivandic *et al.* 2015). The CO_2 plume mainly concentrates around the injection zone. The inferred lateral extent of the CO_2 plume has increased with an increasing amount of injected CO_2. A growth of about 200 m in the E-W direction and 150 m in the N-S direction is observed between the first and second repeat surveys (Ivandic *et al.* 2015). The predominantly westward propagation and asymmetric shape of the CO_2 plume are attributed to the highly heterogeneous reservoir. According to previous studies at the Ketzin site (Ivanova *et al.* 2012; Martens *et al.* 2014; Ivandic *et al.* 2015;

Huang *et al.* 2016), no indication of CO_2 leakage was detected within the caprock, indicating that the injected CO_2 has remained within the saline aquifer.

ACQUISITION AND PROCESSING OF THE FIRST POST-INJECTION SEISMIC SURVEY

As for the acquisition of the previous 3D surveys (Juhlin *et al.* 2007; Ivanova *et al.* 2012; Ivandic *et al.* 2015), the same template scheme (Fig. 3) was utilized for the first post-injection seismic survey. In the first post injection survey, efforts were made to use the same source and receiver locations as the baseline survey. As the anticipated migration of the CO_2 plume is in WNW direction, two new templates, 5:0 and 6:0, serving as an extension of the baseline area, were laid out in the westernmost part of the survey area. However, these two new templates were excluded from the time-lapse processing workflow in this study. Table 1 summarizes the acquisition parameters used for the first post-injection survey. For each template, five receiver lines with twelve perpendicular source lines were utilized. After acquiring data at all sources locations within a template, the receiver lines were shifted. Receiver locations within a Swath (e.g. Templates 5:1, 5:2, 5:3 etc.) had a 50% overlap with the adjacent templates. While source locations for a given template had a 50% overlap with the templates in the adjacent swaths (e.g. Templates 10:1, 9:1, 8:1 etc.). Using this overlapping template scheme, the 3D survey has a nominal fold of 25 for the subsurface area. However, the actual fold (Fig. 4) is less than 25 in some areas as the source was not used in residential/built-up areas or on roads.

Acquisition of the first post-injection survey using a Sercel 428 system started in template 9:5 on September 2, 2015 and was completed in template 2:3 (Fig. 3) on November 14, 2015. During the 58 days of active acquisition, a total number of around 5700 source points were recorded in 33

templates covering an area of approximately 11 km^2. An accelerated weight drop was used, nominally 8 hits were recorded and stacked for each shot point in order to improve the signal to noise ratio. The signal to noise ratio in the data was constantly monitored, in noisy conditions the number of hits were increased.

In order to maximize the repeatability in the time-lapse seismic data, common traces between the baseline and first post-injection surveys were extracted and processed following the same processing workflow applied to the previous 3D surveys (Juhlin *et al.* 2007; Ivanova *et al.* 2012; Ivandic *et al.* 2015). The processing workflow was designed to be comparatively simple to enable fast processing and preservation of the genuine seismic response (Juhlin *et al.* 2007). The processing steps are summarized in Table 2. Detailed explanations for each processing step can be found in Juhlin *et al.* (2007). In spite of all the 3D seismic datasets being acquired using the same acquisition parameters over the same season, differences in velocities of the near-surface are present due to variable weather and ground conditions during the periods of the 3D seismic acquisition (Kashubin *et al.* 2011; Bergmann *et al.* 2014). Accordingly, the static corrections of the first post-injection data need to be re-evaluated. As done in the second repeat survey (Ivandic *et al.* 2015), a time-efficient and data-driven time-lapse difference static correction method presented by Bergmann *et al.* (2014) was applied to the first post-injection survey data, instead of re-picking the first arrivals. The time-shifts were computed using prestack cross-correlation between the baseline and repeat traces in a given time gate. A 50-1100 ms time gate was adopted for the first post-injection survey since after tests it yielded the optimal normalized root-mean-square (NRMS) compared to other time gates. On a surface consistent basis, the time-shifts were decomposed into three parts: source, receiver and CDP solutions. Then the time-lapse difference static corrections were applied to the first post-injection data to match the baseline data.

Although the first post-injection survey was repeated with almost the same acquisition and processing parameters as the baseline survey, there are still some non-injection related factors (e.g., traffic noise, precipitation and positioning error) that can change the seismic amplitude, phase and time, as well as the frequency content (Kashubin *et al.* 2011; Bergmann *et al.* 2014; Huang *et al.* 2016). It is desirable to remove these spurious changes in seismic attributes by performing cross-equalization of the time-lapse seismic datasets. In general, the cross-equalization procedure is implemented using the Pro4D module in the Hampson-Russell software and is composed of the following steps: phase and time matching, phase and frequency shaping by filtering, cross-correlation statics and time-variant shifting, and cross-normalization. A calibration window above the target reservoir zone is used since there should ideally be no injection related time-lapse differences within this interval. The same cross-equalization parameters as applied to the previous time-lapse datasets (Ivandic *et al.* 2012; Ivanova *et al.* 2012; Ivandic *et al.* 2015) were used in order to match the first post-injection dataset to the baseline dataset. In this way, the time-lapse differences obtained by subtracting the repeat volume from the baseline volume can be regarded as changes associated with reservoir property changes. A map of the NRMS change (Fig. 5) between the baseline and first post-injection subvolumes within a time window from 100 ms to 700 ms was extracted to measure the match quality of the time-lapse data after cross-equalization (Kragh and Christie 2002). Higher NRMS values represent lower repeatability, namely larger static shifts and changes in amplitude and phase. It is clearly seen that the majority of the NRMS deviations range from 0.2 to 0.4, indicating that most of the traces have satisfactory repeatability (Miller and Helgerud 2009). Higher NRMS deviations are found at the margins of the survey area where lower S/N is present due to the lower fold. Higher NRMS deviations around the injection area are attributed to the injected CO_2, site operations and lower fold.

4. MIGRATED SECTIONS AND TIME-LAPSE RESULTS

Figure 6 shows time-migrated sections extracted from the baseline and first post-injection volumes along inline 1170 and crossline 1095, which are close to the CO_2 injection well. Like on the baseline sections, the reflections in the range of around 150-900 ms are clearly mapped on the first post-injection sections. The pronounced reflection at approximately 480 ms around the injection area corresponds to the K2 reflector. Consistent seismic reflections can be found on both baseline and repeat sections, whereas stronger amplitudes at about 42 ms beneath the K2 horizon are clearly recognizable on the first post-injection sections. These stronger amplitudes are attributed to the injected CO_2 within the reservoir.

Comparison of the time-lapse amplitude difference sections across the CO_2 injection well for the three repeat surveys are shown in Fig. 7. The obvious amplitude changes between 515 ms and 535 ms TWT denote the presence of the injected CO_2 within the reservoir (Ivanova *et al.* 2012; Ivandic *et al.* 2015). Between the first and second repeat surveys, the amplitude anomaly in the reservoir continued to grow in extent and in amplitude as more CO_2 was injected (Fig. 7). For the first post-injection survey, the range and intensity of the amplitude anomaly within the reservoir has decreased and the push-down effect at deeper levels is weaker compared with the second repeat survey. The most significant decrease in the amplitude anomaly occurs east and south of the injection site. A gradual migration of the plume in the up-dip direction within the reservoir is observed, consistent with the previous results. No anomalies above the K2 are observed.

5. ASSESSMENT OF CO_2 PLUME DISTRIBUTION

To analyze the distribution and migration of the CO_2 plume within the reservoir, the normalized amplitude difference between the baseline and first post-injection surveys was extracted along a

horizon at the top of the reservoir (Fig. 8). The asymmetric distribution of the amplitude anomaly related to the injected CO_2 is clearly recognizable. The peaks of the amplitude anomalies for the first post-injection survey are situated about 120 m west-northwest of the injection well. Compared with the contour lines at the 0.3 level extracted from the previous repeat surveys, the WNW trend of CO_2 migration and the major concentration area of the amplitude anomaly are consistent. The lateral extent of the amplitude anomaly west of the injection site almost coincides with that of the second repeat survey, whereas a marked decrease in size is observed in the eastern and south-eastern parts of the injection area. These features may indicate that the reservoir is quite heterogeneous, especially in the eastern part of the injection area. This is in agreement with the previous interpretation that small-scale heterogeneities are present in the sandstone, especially east of the injection site (Ivandic *et al.* 2015).

A conformity analysis of the observed and simulated CO_2 plume footprint has shown that, according to simulations, a significant amount of CO_2 may be distributed in thin layers which are not detectable by seismic monitoring due to limited vertical resolution (Lüth, Ivanova and Kempka 2015). Since the detectable thickness threshold of the CO_2 plume increases with the presence of time-lapse noise (Lüth *et al.* 2015), it is important to investigate the S/N level in order to objectively assess the CO_2 plume. Maps of S/N of raw prestack shot gathers from the baseline, second repeat and first post-injection surveys were extracted, respectively, as a function of CDP and receiver locations (Kashubin *et al.* 2011). Figure 9 shows the maps of the S/N between the first post-injection and baseline surveys in comparison with the second repeat and baseline surveys. In order not to include ground roll, traces in the offset range between 300 m and 600 m were analyzed. The average absolute amplitude in the window from 0 ms to 150 ms before the first arrivals was considered to be representative of the noise amplitude, whereas the average absolute amplitude in the window from 500 ms to 700 ms (which includes the reservoir) was considered representative of the signal

amplitude (Kashubin *et al.* 2011). The overall S/N level of the first post-injection survey is slightly lower than the second repeat survey at both CDP and receiver locations, probably due to a greater amount of precipitation during the period of the first post-injection acquisition. Therefore, the detection thickness of the gaseous CO_2 plume is expected to be greater in the first post-injection seismic data than that in the second repeat seismic data. In the eastern part of the injection area where a significant decrease in the amplitude anomaly is found in the first post-injection survey, the S/N levels (ranging from 0.4 to 1.0 in CDP location) in the first post-injection survey are lower than those (ranging from 0.6 to 1.0 in CDP location) in the second repeat survey. Therefore, lower S/N levels east of the injection site in the first post-injection survey may be considered as one of the factors contributing to the decrease in the observable CO_2 plume in this area.

4D seismic modelling plays a crucial role in investigating and predicting changes in the seismic response from a reservoir. To better understand the changes in the CO_2 plume, 4D seismic modelling was performed. Previous results of 4D seismic modelling incorporating borehole, 3D seismic data and dynamic flow simulations at the Ketzin site show a reasonable match between the seismic response from the baseline and previous two repeat seismic datasets (Huang *et al.* 2015). In this study, the same modelling approach is used to investigate the change in the seismic response related to the injected CO_2 between the second repeat and first post-injection surveys. A detailed 3D property model for the baseline survey was built by integrating borehole data and a depth model derived from interpretation of the 3D baseline seismic data (Huang *et al.* 2015). The dynamic flow simulations were performed based on an updated static reservoir model for which the observed downhole pressures and the CO_2 arrival times in observation wells had been history matched (Kempka *et al.* 2013; Kempka and Kühn 2013; Norden and Frykman 2013). Given CO_2 density and saturation from dynamic flow simulations, the property model at the time of the first post-injection survey was calculated. Synthetic seismic data for the first post-injection survey were then generated

by convolving the seismic wavelet with the reflection series from the property model. Figure 10 shows the normalized amplitude difference map at the reservoir level from the synthetic seismic data. The outlines of the synthetic amplitude anomalies at the second repeat and first post-injection times are quite close. This is in agreement with the coincident extent of the CO_2 plume west of the injection site observed in the field data (Fig. 8). Figure 11 shows the CO_2 balance from the reservoir simulations and the corresponding CO_2 dissolution ratio. Relatively high CO_2 dissolution rates, up to about 27 % at the relevant times, are observed in the simulations. This dissolved CO_2 is undetectable for seismic time-lapse measurements. In addition, the flow simulations also indicate that the areal extent of thin layers in 2015 is larger by 30% than in 2012 due the process of the CO_2 diffusion. This implies that during the first post-injection time, there is a dynamic balance between newly injected CO_2 (6 kt more injected after the second repeat time) and that being dissolved and diffused.

When comparing between the synthetic and field datasets, it is clear that the extent of the CO_2 plume in the synthetic dataset is larger than that in the field dataset. Apart from our limited knowledge about the heterogeneous reservoir, another reason for this discrepancy is that the synthetic dataset is noise-free, resulting in a smaller detectable thickness of the CO_2 plume compared with data including noise. The minimum thickness of gaseous CO_2 plume which can be imaged is 6.5 m in the second repeat seismic data (Lüth *et al.* 2015). Due to slightly lower signal to noise ratio in the first post-injection survey than in the second repeat survey, the minimum thickness of gaseous CO_2 plume which can be imaged is expected to be 7 m or greater. Therefore, a threshold of 7 m CO_2 thickness was applied when extracting the amplitude difference horizon from the synthetic seismic data at the time of the first post-injection survey (Fig. 10). Compared with the synthetic result without applying the threshold, the extent of the synthetic anomaly is closer to that of the field data, but some discrepancies are still present. Table 3 shows the detectable mass of gaseous CO_2 calculated from simulations with the corresponding CO_2 thickness threshold. It is clear

that the gaseous CO_2 plume is thinning. This indicates that the discrepancy between the detectable mass of the gaseous CO_2 plume and total CO_2 mass for the first post-injection survey is mainly due to the CO_2 dissolution and the process of the CO_2 diffusion.

6. CO_2 SATURATION CONDITIONS CALCULATED FROM PNG LOGGING DATA

Information about in-situ CO_2 saturation conditions was retrieved from pulsed neutron-gamma (PNG) well-log data, as well as from the interpretation of the two previous 3D seismic repeats. New PNG logging data acquired close to the time of the 2015 post-injection survey have been evaluated using the approach for calculating CO_2 saturations and PNG processing parameters described in Ivandic *et al.* (2015). PNG logging has also been applied successfully at other sites for measuring saturation conditions during injection of CO_2, e.g. for investigation of residual trapping at the Otway site (Dance and Paterson 2016), underpinning the applicability of the technique for this type of study.

PNG tools radiometrically measure the macroscopic capture cross-section Σ (Plasek *et al.* 1995). The formation Σ value is equal to the volume-weighted average of the Σ values of the matrix components and the fluids filling the pore space. In time-lapse mode, changes of saturation S can be calculated from the Σ change between baseline and repeat logging runs, where the Σ difference is attributed to the change of pore fluids (Ellis and Singer 2007):

$$S_{w,base} - S_{w,log} = \frac{\Sigma_{base} - \Sigma_{log}}{\phi\left(\Sigma_w - \Sigma_g\right)},$$

(1)

where the subscripts *log* and *base* refer to the repeat and baseline logging runs, and ϕ is formation porosity. For the current application, the subscripts w and g correspond to the pore fluids, brine and

CO_2, and the CO_2 saturation is equal to the change in brine saturation, $S_{w,base}$ - $S_{w,log}$. For the current study, 97.6 cu and 0.014 cu are used for the fluid parameters Σ_w and Σ_g, respectively. Total porosity values derived from open-hole logging data after Norden *et al.* (2010) have been used, which is similar to our evaluation of the PNG data for the previous 3D seismic repeat survey described in Ivandic *et al.* (2015). As no indications for salt precipitation were observed in the post-injection phase, saturation was computed assuming displacement of brine by CO_2 only, and effects of salt precipitation were not considered. Further details on PNG logging and interpretation at Ketzin can be found in Baumann, Henninges and De Lucia (2014).

PNG logs were acquired in October 2015 in the observation wells Ktzi 200 (R9) and Ktzi 203 (R5) using the Reservoir Saturation Tool (RST) from Schlumberger. Similar processing and environmental corrections as for previous logging runs were applied. Therefore the PNG data of different runs can be directly compared. Nevertheless, the boreholes available for logging have changed: The new well Ktzi 203 drilled in 2012 (Prevedel *et al.* 2014) has now been included in the PNG logging campaign. No data from former observation well Ktzi 202 could be collected, due to its final abandonment in 2015. No logs could be acquired in the former injection well Ktzi 201 due to operational reasons in October 2015, data from the previous repeat in October 2014 (R8) have been considered for this well in the present study.

PNG logs and calculated CO_2 saturations for Ktzi 200, Ktzi 201, and Ktzi 203, which are representative for the 2015 3D seismic repeat are presented in Fig. 12. Data from the baseline runs (B) and for the time of the previous 3D seismic repeat in 2012 are displayed for comparison and in order to visualize the evolution of saturation conditions. For time-lapse PNG evaluation in Ktzi 203, no baseline data are available, as the reservoir was already filled with CO_2 when the well was drilled. As very close agreement of lithological and petrophysical properties can be observed, both baseline PNG and

open-hole porosity data for Ktzi 201 have been used for evaluation of the Ktzi 203 repeat PNG data. Due to the up-dip position of Ktzi 203 relative to Ktzi 201 within the Ketzin anticline, a depth shift of 2.1 m upwards has been applied to the Ktzi 201 data for this purpose.

Average CO_2 saturations calculated for individual lithological units are listed in Table 4 (see Fig. 12 for position of units). The PNG log data indicate that CO_2 is once again predominantly present in the upper sandstone layer of the storage interval (denoted as unit 1). Compared to 2012, there is a general tendency towards lower saturations at the bottom, and increased saturations at the top of the CO_2 plume. This is interpreted as a rise of the CO_2 plume due to buoyancy forces which has occurred after injection was stopped in August 2013. This is in agreement with a trend already observed during a longer shut-in period before the end of the injection in 2013 (Baumann *et al.* 2014). The highest CO_2 saturations, with an average of 64 % occur at Ktzi 203, whereas lower CO_2 saturations are observed in Ktzi 201 and 200, also compared to 2012. This indicates that the CO_2 plume is moving away from the injection point in the up-dip direction.

In contrast to this general tendency towards an upward movement of the CO_2 plume, there is also evidence for the presence of CO_2 within a thinner sand and silt layer some meters below the main injection interval in the Ktzi 201 well (units 3 and 4). Here, CO_2 had been detected earlier, during the injection phase (Baumann *et al.* 2014), at the time of the first 3D seismic repeat (Ivanova *et al.* 2012). However, it was not detected during 2012 (see Fig. 12). With respect to the lateral extent of this deeper CO_2 interval it should be noted that Ktzi 203 is only accessible to about 640 m depth, due to a blockage of the well with cement, and no PNG data is available from the intervals below. There are nevertheless indications of the presence of CO_2 from gas measurements performed on core samples below this depth in Ktzi 203 (Barth *et al.* 2015).

7. QUANTITATIVE INTERPRETATION OF THE TIME-LAPSE SEISMIC SIGNATURE

Approaches for a quantitative interpretation of seismic time-lapse signatures have been presented and discussed as an important component for the safety assessment of a storage site (Ghaderi and Landrø 2009; Chadwick *et al.* 2010; Grude *et al.* 2014; Lüth *et al.* 2015).

Ivanova *et al.* (2012) and Ivandic *et al.* (2015) quantified the amount of CO_2 visible in two 3D time-lapse seismic repeat surveys in 2009 and 2012 while CO_2 was being injected at the Ketzin pilot site. They used a logging-seismic approach (Ivanova *et al.* 2012) composed of two main steps (Fig. 13). First, CO_2 saturations (S_{CO2}) are inferred from time-lapse amplitude changes, ΔA (Fig. 8). For this purpose, Ivanova *et al.* (2012) and Ivandic *et al.* (2015) used PNG logs from three wells at Ketzin in order to derive a relationship between S_{CO2} and ΔA. Once the saturation levels are mapped out over the survey area, the second step consists of analyzing the time shifts (Δt) for CO_2 layer thickness (h) of each CDP bin by the following equation:

$$ h = \Delta t \cdot \frac{v_1 \cdot v\left(S_{CO_2}\right)}{2 \cdot \Delta v}, $$

(2)

where Δt is the time-delay of reflections in each CDP bin below the reservoir due to reduced velocities of CO_2 saturated strata (Arts *et al.* 2004), v_1 is the reservoir velocity fully saturated with brine, $v(S_{CO2})$ is the reservoir velocity for the specified CO_2 saturation value (S_{CO2}) in each CDP bin and Δv is equal to $v_1 - v(S_{CO2})$. Subsequently $v(S_{CO2})$ will be referred to S_{CO2} as a linear velocity-saturation relationship. The total mass of CO_2 (M_{tot}) is then computed by summation of the CO_2 mass concentrations in all the CDP bins with the following equation:

$$ M_{tot} = \sum_{i=1}^{N} h \cdot S_{CO_2} \cdot \phi \cdot \rho \cdot dx \cdot dy, $$

(3)

where i is the CDP index, $\varnothing$ is the porosity, ρ is the CO_2 density, $dx \cdot dy$ is the CDP bin area and N is total number of CDPs.

The estimates made by the method of Ivanova *et al.* (2012) are affected by considerable uncertainties (Ivanova *et al.* 2012; Bergmann and Chadwick 2015; Ivandic *et al.* 2015). In this study we apply the same quantification approach to the first post-injection seismic survey and discuss visible post-injection changes in CO_2 plume behavior.

Seismic input parameters for the present estimation comprise (a) differences of the normalized seismic amplitudes between the first post-injection and baseline surveys at Ketzin (Juhlin *et al.* 2007) (Fig. 8) and (b) time-delays between these surveys due to the velocity pushdown effect (Fig. 14) evaluated by calculating differences of the time shifts between the baseline and first post-injection signals within the windows above and below the reservoir horizon. In this quantification study, time-lapse changes in the seismic data (Fig. 8, Fig. 14) are considered to be due to the fluid saturation effects (CO_2/brine) only. We assume that possible effects of pore pressure on the seismic data at the Ketzin pilot site can be neglected (Ivanova *et al.* 2013a). It should be noted that there are no pronounced time-delays near the injection well (Fig. 14) despite the presence of amplitude anomalies (Fig. 8). This is probably due to the impact of brine injection in the CO_2 storage formation which commenced on 12 Oct 2015 (Möller, Liebscher and Schmidt-Hattenberger 2016), after the CO_2 injection was terminated.

CO_2 mass calculations are performed under the assumed reservoir conditions at Ketzin in the fall 2015. The value for CO_2 density (184.2 kg/m³) is obtained after Span and Wagner (1996) using pressure/temperature data measured in the reservoir in October 2015. In this study CO_2 density and

porosity of the reservoir are assumed to be constant for the entire reservoir. A reservoir porosity of 20% is assumed after Förster *et al.* (2010). A petrophysical model for compressional velocity change in the reservoir due to CO_2 fluid substitution (the pushdown effect) was derived by Ivanova *et al.* (2013b). The baseline compressional velocity value (100% brine saturation in the reservoir) is 3135 m/s after Ivanova *et al.* (2012). The shear velocity is assumed to remain constant according to Kummerow and Spangenberg (2011).

In order to provide a consistent methodology for estimating the observable CO_2 mass, we use here the same saturation model for all three repeat surveys. Ivanova *et al.* (2012) and Ivandic *et al.* (2015) used CO_2 saturations based on the PNG logging data when performing their calculations. Here we use the CO_2 saturation versus amplitude difference from the first repeat survey. These saturations are similar to what is observed on the PNG logs (Table 4), but do not correspond exactly to them. The amplitude difference and time delay cutoffs are the same as for the 2009 and 2012 surveys. Only a different pressure/temperature is assumed for the 2015 survey (resulting in a lower density for the CO_2). Applying equation (3) then gives a total observable CO_2 mass of 10.8 kt. This is only about 16% of the total injected CO_2 mass. For completeness we also show in Table 5 the estimated CO_2 mass for the other two surveys using consistent input parameters and the estimates made by Ivanova *et al.* (2012) for the first repeat and Ivandic *et al.* (2015) for the second repeat. The difference between the estimate in this study for the first repeat and that presented in Ivanova *et al.* (2012) can be attributed to interpolation from geographic coordinates. If the saturation relationship from the new PNG logging data (Table 4) and the same cutoff values are used as in Ivandic *et al.* (2015) for the post-injection survey, then the observable CO_2 mass is 13 kt, still considerably lower than the injected amount.

Figure 15 shows the CO_2 mass for the three seismic repeat surveys estimated in this study using

consistent input parameters. The percentage of detected CO_2 is dramatically lower for the third repeat than for the two surveys acquired during the injection period (85-90%). Apart from limited understanding of the highly heterogeneous reservoir, possible explanations are, as discussed earlier, limited vertical resolution of the seismic monitoring, lower S/N, CO_2 dissolution and diffusion. Given that the percentage of CO_2 that is expected to be observable also decreases significantly with time in the simulations (Table 3), the observed low percentage for the first post-injection survey is not unreasonable. CO_2 dissolution and the process of CO_2 diffusion (thinning of the gaseous CO_2 layer) are most likely the main factors contributing to the significant decrease. In addition, the influence of the brine injection may have some impact on the time-delays in the near wellbore zone (Fig. 14).

Note that the amount of gaseous CO_2 was overestimated in both the first and second repeat surveys (compare values in Table 3 and Table 5). This suggests that the CO_2 saturation functions assumed based on the PNG logs are not representative for the entire reservoir.

The impact of various uncertain reservoir parameters on the CO_2 mass estimate of the first injection survey is shown in Fig. 16. The different choices of input values result in distinct uncertainties of the estimated mass. The estimated mass is more sensitive to the choices of time-delay cutoff and reservoir velocity, whereas the choice of the time-lapse amplitude difference cutoff plays a minor role. For instance, an increase of 10% in the time-delay cutoff and reservoir velocity fully saturated with brine leads to a 48.7% and a 23.2% increase in mass, respectively, whereas the same increase in the amplitude difference cutoff only leads to a 0.3% increase. A change of 10% in porosity results in a change of 10% in mass. These uncertainties can be more significant due to oversimplification for the highly heterogeneous reservoir, limited number of petrophysical observations and upscaling errors from petrophysical scale to seismic scale.

8. VOLUMETRIC BOUNDS USING NON-PATCHY SATURATION MODELS

The mass estimation presented in the chapter "Quantitative Interpretation of the Time-lapse Seismic Signature" relies on two main assumptions: (1) CO_2 saturations can be reliably estimated from time-lapse amplitude differences and (2) chosen thresholds for time-lapse amplitudes and time shifts are accurate. Apart from these assumptions, Fig. 16 shows that the mass estimation is most susceptible to errors in the velocity parameters from the petrophysical model. The accuracy of CO_2 mass estimation therefore depends significantly on the validity of the velocity-saturation relationship. For Ketzin, the petrophysical model contains a number of uncertainties arising from the fact that (1) only a limited number of core samples were available for petrophysical experiments, (2) the reservoir lithology is heterogeneous, and (3) the ultra-sonic frequencies used in the laboratory experiments are different from those relevant for the surface-seismic experiments.

Ivanova *et al.* (2012) report that the saturation-dependent velocities follow the trend of a patchy saturation model and use a linear velocity-saturation relationship. In particular, they use a relationship that is interpreted for CO_2 saturation levels of up to 51%. In a similar way, Ivanova *et al.* (2013b) present a relationship which obeys

$$\frac{\Delta v}{v_p} = -0.46 \cdot S_{CO_2}.$$

(4)

Together with a starting velocity of v_l=3135 m/s, the corresponding velocity-saturation relationship then reads

$$v_p\left(S_{CO_2}\right) = -1442 \cdot S_{CO_2} + 3135.$$

(5)

Figure 17 shows this relationship together with the laboratory data it has been fitted from. Given that the laboratory data reach CO_2 saturations of up to 55 %, it appears questionable whether a linear patchy saturation model is the only possible scenario to be considered in CO_2 mass quantification. A Gassmann-type model, for instance, might result in a similar fit to the laboratory data, but may flatten out to higher velocities for large CO_2 saturations. This is of relevance since CO_2 saturations in excess of 60 % have been observed from PNG measurements (Ivanova *et al.* 2012). In addition, Baumann *et al.* (2014) report that the maximum CO_2 saturation at Ktzi 201 was 68% on average and reached 100% locally.

The following analysis is therefore addressing the question of whether the so far applied patchy saturation model can really be considered as the only possible model for volumetric interpretation. For this purpose, volumetric interpretation will be revisited using an alternative approach to that applied in the previous section. This alternative approach is based on 4D time shifts and the petrophysical model solely (Bergmann and Chadwick 2015), whereas the previously applied approach depends also on 4D amplitude changes and logged CO_2 saturation levels. For clarity, the approach of the previous section will subsequently be referred to as the logging-seismic approach, and the alternative approach will be referred to as the time-shift approach.

8.1 CO_2 MASS ESTIMATION USING THE TIME-SHIFT APPROACH

Similar to the logging-seismic approach, this second approach is based on equation 2. After rearranging the equation for the time shift, Δt, it is clear that the combination of CO_2 saturation and layer thickness produces a specific time shift which is not unique with respect to the mass of CO_2 in the layer. That is, two different layers, e.g. one thin layer with high CO_2 saturation and a second layer with larger thickness but lower CO_2 saturation, can yield an identical time shift. However, both layers have different masses of CO_2 contained within them.

In order to compute the range of possible CO_2 masses in the layer, Bergmann and Chadwick (2015) proposed the generalized velocity-saturation relationship

$$v(s_2) = v_1 + \left(1 - \frac{p\left(1 - S_{CO_2}\right)}{p + S_{CO_2}}\right) \cdot \Delta v$$

(6)

that is parameterized by the patchiness parameter p and the velocity change Δv. The velocity change is given by the difference of the velocities for full CO_2 saturation, $v_2 = v(S_{CO2}=1)$, and full brine saturation, i.e. $\Delta v = v_2 - v_1$.

Figure 18 shows that the patchiness parameter is specifying the degree of linearity in the velocity-saturation relationship. Once this generalized velocity-saturation relationship is fitted to a pre-existing petrophysical model, observed 4D time shifts can be converted into lower and upper CO_2 mass bounds. In accordance to equation 3, we report these bounds here in reference to the total mass of CO_2 as

$$M_1 = -(dx \cdot dy) \cdot \frac{\rho_2 \cdot \phi \cdot v_1 \cdot (v_1 + \Delta v)}{2\Delta v} \cdot \sum_{i=1}^{N} \Delta t_i$$

(7)

and

$$M_2 = -(dx \cdot dy) \cdot \sum_{i=1}^{N} \frac{\rho_2 \cdot \phi \cdot p \cdot v_1^2 \cdot h_{max}}{\left(\Delta v \cdot (p+1) + v_1\right) \cdot v_1 \cdot \Delta t_i + 2(p+1) \cdot \Delta v \cdot h_{max}} \cdot \Delta t_i \, ,$$

(8)

where h_{max} is the maximum CO_2 layer thickness set by the reservoir thickness.

For velocity-saturation relationships with patchiness parameters lower than $p_{lin} = -(v_1 + \Delta v)/\Delta v$, M_1 constitutes the upper total mass bound and M_2 the lower total mass bound. In turn, for $p > p_{lin}$, M_1 and M_2 constitute the lower and upper total mass bounds, respectively. Figure 19 gives a comparison of the two approaches for the Ketzin data. The estimated CO_2 mass using the logging-seismic approach generally lies between M_1 and M_2 bounds.

8.2 APPLICATION AND DISCUSSION

In order to investigate the possible presence of a non-patchy saturation model, we use the time-shift approach to recompute mass estimations for variable velocity-saturation relationships. To validate the individual velocity-saturation relationships, we then compare the recomputed CO_2 mass estimates to the true amount of CO_2 injected. For this purpose, the patchiness parameter is logarithmically varied between 0.1 and 10, and the velocity change linearly varied between -1635 m/s and -635 m/s. Within these ranges, the linear model used by Ivanova *et al.* (2013b) (see equation 4) is approximated by a relatively high velocity change (i.e., -1442 m/s) and a patchiness parameter of 10. For consistency with previous mass estimations, we apply the same 4D amplitude thresholding (see Table 5) as has been conducted in previous studies (Ivanova *et al.* 2012; Ivandic *et al.* 2015). As an additional measure for bias removal of the time shifts, a mean time shift was computed outside the 4D amplitude signature, which was then subtracted from the amplitude-thresholded time shifts.

Variation of the patchiness parameter and the velocity change leads to the total mass bounds M1 and M2 shown in Fig. 20a-b. As an example, for the linear model used by Ivanova *et al.* (2013b), e.g. Δv =-1442 m/s and p=10, the CO_2 mass can be inferred to approximately lie between M1=21 kilotons and M2=36 kilotons. Those scenarios for which the M1 and M2 bounds are in agreement with the true amount of CO_2 injected are deemed to be based on a plausible velocity-saturation relationship. More specifically, in order for a velocity-saturation relationship to be considered as valid, the true amount of CO_2 must be contained within the mass interval spanned by the corresponding M1 and M2 bounds (Fig. 20c). Figure 21 specifically shows the respective velocity-saturation relationships, from which the following observations are made:

- Generally, the set of plausible velocity-saturation models is not limited to linear models.

- Moderate Gassmann-type models (with end-member-velocities greater than 2000 m/s) are plausible too, whereas more pronounced Gassmann-type models (with end-member-velocities lower than 2000 m/s) can be mostly excluded.

Apart from providing consistent mass estimations, the moderate Gassmann-type models appear to correlate to the laboratory data visually in a similar quality as the relationship after Ivanova *et al.* (2012). However, performing a quantitative correlation is difficult because individual errors for the laboratory data are not available.

Considering the probability of higher end-member velocities, i.e. velocities at full CO_2 saturation, this would imply that CO_2 masses are potentially overestimated for regions with average CO_2 saturations greater than 50 %. Given the results from the PNG logging (Baumann *et al.* 2014), it is clear, however, that this region will be confined to the area near the injection well. It is therefore expected that the variability of the possible velocity-saturation relationships will have a rather limited impact on the total mass estimates from the logging-seismic approach.

9. DISCUSSION AND CONCLUSIONS

Time-lapse reflection seismic monitoring has proven to be effective and important for mapping changes in the reservoir and potential leakage after CO_2 injection at the Ketzin site. Using the same acquisition parameters as in the previous 3D surveys, the first post-injection survey was acquired in autumn 2015. A consistent processing flow was used for all the 3D datasets. The time-migrated sections and maps of the NRMS error reveal that repeatability between the baseline and first post-injection datasets is high. The results of the time-lapse analysis highlight the CO_2 induced changes in seismic responses between 515 ms and 535 ms TWT. The injected CO_2 remains within the reservoir,

verifying the reservoir integrity. Compared with the vertical sections of the time-lapse amplitude differences from the second repeat survey, a decrease in intensity and in the extent of the amplitude anomaly at the first post-injection time is observed in both the horizontal and vertical directions. In addition, a consistent tendency of movement of the plume in the up-dip direction is seen. Like the previous time-lapse results, the amplitude difference horizon of the first post-injection survey reveals a predominant WNW tendency in the migration of the CO_2 plume. The heterogeneous distribution of the CO_2 plume west of the injection site is comparable to that at the second repeat time even though 6 kt of additional CO_2 were injected after the second repeat survey. The reduced anomaly may be partly due to CO_2 diffusion, which would act to reduce the thickness of the gaseous CO_2 layer below the seismic detection limit in some areas. 4D seismic modelling based on the dynamic flow simulations also show that the synthetic amplitude differences should be similar for the second repeat and first post-injection times, implying that a dynamic balance between the CO_2 injected after the second repeat survey and the CO_2 undergoing dissolution/diffusion is achieved at the time of the first post-injection survey. CO_2 dissolution ratios of up to 27 % are observed in the simulations. This is reasonable due to the presence of the extensive CO_2-brine interface in the heterogeneous reservoir and the relatively low injection rates. It is very likely that more active CO_2 dissolution is present east of the injection site due to lower CO_2 flow rates and rock permeabilities. In addition, significant decreases in the amplitude anomaly east of the injection site could be due to lower S/N level in this area, leading to an increase in the thickness of the seismic detection limit. Therefore, the decrease in the amplitude anomaly at the Ketzin pilot site may be due to multiple factors. Further investigation by combining other geophysical methods and fluid flow simulations may shed light on the processes.

The quantitative interpretation of the first post-injection 3D seismic survey demonstrates considerable post-injection changes in the CO_2 plume behavior at Ketzin. Notable uncertainties

remain in the quantitative interpretation using the logging-seismic approach due to uncertain reservoir parameters. As an alternative, a time-shift approach is also performed to define the lower and upper CO_2 mass estimates. Our studies imply that CO_2 masses are probably overestimated for regions with average CO_2 saturations greater than 50 %. In addition to complex reservoir properties, the increased mismatch between the estimated and injected CO_2 mass at the first post-injection time can also be attributed to factors like the limited vertical resolution of the seismic monitoring, lower S/N, brine injection, CO_2 dissolution and diffusion. In terms of CO_2 dissolution and diffusion, both processes demonstrate ongoing stabilization of the CO_2 plume. Dissolution is an important trapping mechanism in the early post-closure phase, when mineral trapping does not yet contribute strongly to overall trapping (Rochelle, Czernichowski-Lauriol and Milodowski 2004; Kempka, De Lucia and Kühn 2014). The accumulation of CO_2 in rather thin layers is an indication of ongoing pressure relaxation in the reservoir since the CO_2 would rather propagate with larger plume thickness at a higher reservoir pressure. Simulations imply that the CO_2 dissolution and the process of CO_2 diffusion are the main factors that account for the significant discrepancy between the injected and estimated CO_2 mass for the first post-injection survey.

ACKNOWLEDGEMENTS

REFERENCES

Arts R., Eiken O., Chadwick A., Zweigel P., Van der Meer L. and Zinszner B. 2004. Monitoring of CO_2 injected at Sleipner using time-lapse seismic data. *Energy* **29**, 1383-1392.

Barth J., Nowak M., Zimmer M., Norden B. and van Geldern R. 2015. Monitoring of cap-rock integrity during CCS from field data at the Ketzin pilot site (Germany): Evidence from gas composition and stable carbon isotopes. *International Journal of Greenhouse Gas Control* **43**, 133-140.

Baumann G., Henninges J. and De Lucia M. 2014. Monitoring of saturation changes and salt precipitation during CO_2 injection using pulsed neutron-gamma logging at the Ketzin pilot site. *International Journal of Greenhouse Gas Control* **28**, 134-146.

Bergmann P. and Chadwick A. 2015. Volumetric bounds on subsurface fluid substitution using 4D seismic time shifts with an application at Sleipner, North Sea. *Geophysics* **80**, B153-B165.

Bergmann P., Kashubin A., Ivandic M., Lüth S. and Juhlin C. 2014. Time-lapse difference static correction using prestack crosscorrelations: 4D seismic image enhancement case from Ketzin. *Geophysics* **79**, B243-B252.

Bergmann P., Yang C., Lüth S., Juhlin C. and Cosma C. 2011. Time-lapse processing of 2D seismic profiles with testing of static correction methods at the CO_2 injection site Ketzin (Germany). *Journal of Applied Geophysics* **75**, 124-139.

Chadwick A., Williams G., Delepine N., Clochard V., Labat K., Sturton S., Buddensiek M.-L., Dillen M., Nickel M. and Lima A.L. 2010. Quantitative analysis of time-lapse seismic monitoring data at the Sleipner CO_2 storage operation. *The Leading Edge* **29**, 170-177.

Dance T. and Paterson L. 2016. Observations of carbon dioxide saturation distribution and residual trapping using core analysis and repeat pulsed-neutron logging at the CO2CRC Otway site. *International Journal of Greenhouse Gas Control* **47**, 210-220.

Ellis D.V. and Singer J.M. 2007. Well logging for earth scientists, 2nd ed, p. 692. Springer. ISBN 1402046022.

Förster A., Norden B., Zinck-Jrgensen K., Frykman P., Kulenkampff J., Spangenberg E., Erzinger J., Zimmer M., Kopp J. and Borm G. 2006. Baseline characterization of the CO_2SINK geological storage site at Ketzin, Germany. *Environmental Geosciences* **13**, 145-161.

Förster A., Schöner R., Förster H.-J., Norden B., Blaschke A.-W., Luckert J., Beutler G., Gaupp R. and Rhede D. 2010. Reservoir characterization of a CO_2 storage aquifer: the Upper Triassic Stuttgart Formation in the Northeast German Basin. *Marine and Petroleum Geology* **27**, 2156-2172.

Ghaderi A. and Landrø M. 2009. Estimation of thickness and velocity changes of injected carbon dioxide layers from prestack time-lapse seismic data. *Geophysics* **74**, O17-O28.

Grude S., Landrø M., White J. and Torsæter O. 2014. CO_2 saturation and thickness predictions in the Tubåen Fm., Snøhvit field, from analytical solution and time-lapse seismic data. *International Journal of Greenhouse Gas Control* **29**, 248-255.

Hansen O., Gilding D., Nazarian B., Osdal B., Ringrose P., Kristoffersen J.-B., Eiken O. and Hansen H. 2013. Snøhvit: the history of injecting and storing 1 Mt CO_2 in the Fluvial Tubåen Fm. *Energy Procedia* **37**, 3565-3573.

Huang F., Juhlin C., Han L., Sopher D., Ivandic M., Norden B., Deng W., Zhang F., Kempka T. and Lüth S. 2016. Feasibility of utilizing wavelet phase to map the CO_2 plume at the Ketzin pilot site,

Germany. *Geophysical Prospecting*, doi: 10.1111/1365-2478.12383, in press.

Huang F., Juhlin C., Kempka T., Norden B. and Zhang F. 2015. Modeling 3D time-lapse seismic response induced by CO_2 by integrating borehole and 3D seismic data – A case study at the Ketzin pilot site, Germany. *International Journal of Greenhouse Gas Control* **36**, 66-77.

Ivandic M., Juhlin C., Lüth S., Bergmann P., Kashubin A., Sopher D., Ivanova A., Baumann G. and Henninges J. 2015. Geophysical monitoring at the Ketzin pilot site for CO_2 storage: New insights into the plume evolution. *International Journal of Greenhouse Gas Control* **32**, 90-105.

Ivandic M., Yang C., Lüth S., Cosma C. and Juhlin C. 2012. Time-lapse analysis of sparse 3D seismic data from the CO_2 storage pilot site at Ketzin, Germany. *Journal of Applied Geophysics* **84**, 14-28.

Ivanova A., Bergmann P., Kummerow J., Yang C., Lüth S. and Juhlin C. 2013a. Seismic Modeling of the AVO/AVA Response to CO_2 Injection at the Ketzin Site, Germany. *Energy Procedia* **40**, 490-498.

Ivanova A., Juhlin C., Lengler U., Bergmann P., Lüth S. and Kempka T. 2013b. Impact of temperature on CO_2 storage at the Ketzin site based on fluid flow simulations and seismic data. *International Journal of Greenhouse Gas Control* **19**, 775-784.

Ivanova A., Kashubin A., Juhojuntti N., Kummerow J., Henninges J., Juhlin C., Lüth S. and Ivandic M. 2012. Monitoring and volumetric estimation of injected CO_2 using 4D seismic, petrophysical data, core measurements and well logging: a case study at Ketzin, Germany. *Geophysical Prospecting* **60**, 957-973.

Juhlin C., Giese R., Zinck-Jørgensen K., Cosma C., Kazemeini H., Juhojuntti N., Lüth S., Norden B. and Förster A. 2007. 3D baseline seismics at Ketzin, Germany: the CO_2SINK project. *Geophysics* **72**, B121-B132.

Kashubin A., Juhlin C., Malehmir A., Lüth S., Ivanova A. and Juhojuntti N. 2011. A footprint of rainfall on land seismic data repeatability at the CO_2 storage pilot site, Ketzin, Germany. 81st SEG Annual Meeting, San Antonio, USA, SEG Expanded Abstract, pp. 4165-4169.

Kazemeini S.H. 2009. Seismic Investigations at the Ketzin CO_2 Injection Site, Germany: Applications to Subsurface Feature Mapping and CO_2 Seismic Response Modeling. PhD thesis, Uppsala University.

Kempka T., Class H., Görke U.-J., Norden B., Kolditz O., Kühn M., Walter L., Wang W. and Zehner B. 2013. A dynamic flow simulation code intercomparison based on the revised static model of the Ketzin pilot site. *Energy Procedia* **40**, 418-427.

Kempka T., De Lucia M. and Kühn M. 2014. Geomechanical integrity verification and mineral trapping quantification for the Ketzin CO_2 storage pilot site by coupled numerical simulations. *Energy Procedia* **63**, 3330-3338.

Kempka T. and Kühn M. 2013. Numerical simulations of CO_2 arrival times and reservoir pressure coincide with observations from the Ketzin pilot site, Germany. *Environmental Earth Sciences* **70**, 3675-3685.

Kragh E. and Christie P. 2002. Seismic repeatability, normalized rms, and predictability. *The Leading Edge* **21**, 640-647.

Kummerow J. and Spangenberg E. 2011. Experimental evaluation of the impact of the interactions of CO_2-SO_2, brine, and reservoir rock on petrophysical properties: A case study from the Ketzin test site, Germany. *Geochemistry, Geophysics, Geosystems* **12**, Q05010.

Lüth S., Ivanova A. and Kempka T. 2015. Conformity assessment of monitoring and simulation of CO_2 storage: A case study from the Ketzin pilot site. *International Journal of Greenhouse Gas Control* **42**, 329-339.

Möller F., Liebscher A. and Schmidt-Hattenberger C. 2016. Report on the dataset of the Brine Injection at the CO_2 Storage Pilot Site Ketzin, Germany. Scientific Technical Report STR; 16/05, Potsdam: GFZ German Research Centre for Geosciences, doi: 10.2312/GFZ.b103-16059.

Martens S., Kempka T., Liebscher A., Lüth S., Möller F., Myrttinen A., Norden B., Schmidt-Hattenberger C., Zimmer M. and Kühn M. 2012. Europe's longest-operating on-shore CO_2 storage site at Ketzin, Germany: a progress report after three years of injection. *Environmental Earth Sciences* **67**, 323-334.

Martens S., Möller F., Streibel M., Liebscher A. and the Ketzin Group. 2014. Completion of five years of safe CO_2 injection and transition to the post-closure phase at the Ketzin pilot site. *Energy*

Procedia **59**, 190-197.

Miller A.C. and Helgerud M.B. 2009. 4D Seismic Repeatability: Lessons From Hoover-Madison-Marshall. 79th SEG Annual Meeting, Houston, USA, SEG Expanded Abstract, pp. 3884-3888.

Norden B., Förster A., Vu-Hoang D., Marcelis F., Springer N. and Le Nir I. 2010. Lithological and petrophysical core-log interpretation in CO_2SINK, the European CO_2 onshore research storage and verification project. *SPE Reservoir Evaluation & Engineering* **13**, 179-192.

Norden B. and Frykman P. 2013. Geological modelling of the Triassic Stuttgart Formation at the Ketzin CO_2 storage site, Germany. *International Journal of Greenhouse Gas Control* **19**, 756-774.

Plasek R., Adolph R., Stoller C., Willis D., Bordon E. and Portal M. 1995. Improved pulsed neutron capture logging with slim carbon-oxygen tools: Methodology, SPE Annual Technical Conference and Exhibition. Society of Petroleum Engineers, Dallas, Texas, p. 15.

Prevedel B., Martens S., Norden B., Henninges J. and Freifeld B.M. 2014. Drilling and Abandonment Preparation of CO_2 storage wells–Experience from the Ketzin pilot site. *Energy Procedia* **63**, 6067-6078.

Ringrose P., Mathieson A., Wright I., Selama F., Hansen O., Bissell R., Saoula N. and Midgley J. 2013. The In Salah CO_2 storage project: lessons learned and knowledge transfer. *Energy Procedia* **37**, 6226-6236.

Rochelle C., Czernichowski-Lauriol I. and Milodowski A. 2004. The impact of chemical reactions on CO_2 storage in geological formations: a brief review. *Geological Society, London, Special Publications* **233**, 87-106.

Span R. and Wagner W. 1996. A new equation of state for carbon dioxide covering the fluid region from the triple-point temperature to 1100 K at pressures up to 800 MPa. *Journal of physical and chemical reference data* **25**, 1509-1596.

Stocker T., Qin D., Plattner G., Tignor M., Allen S., Boschung J., Nauels A., Xia Y., Bex B. and Midgley P. 2013. Climate Change 2013: The Physical Science Basis. Cambridge University Press. ISBN 978-1-107-05799-0.

Xu Z., Juhlin C., Gudmundsson O., Zhang F., Yang C., Kashubin A. and Lüth S. 2012. Reconstruction of subsurface structure from ambient seismic noise: an example from Ketzin, Germany. *Geophysical Journal International* **189**, 1085-1102.

Yang C., Juhlin C., Enescu N., Cosma C. and Lueth S. 2010. Moving source profile data processing, modelling and comparison with 3D surface seismic data at the CO_2SINK project site, Ketzin, Germany. *Near Surface Geophysics* **8**, 601-610.

Yordkayhun S., Juhlin C., Giese R. and Cosma C. 2007. Shallow velocity–depth model using first arrival traveltime inversion at the CO_2SINK site, Ketzin, Germany. *Journal of Applied Geophysics* **63**, 68-79.

Zhang F., Juhlin C., Cosma C., Tryggvason A. and Pratt R.G. 2012. Cross-well seismic waveform tomography for monitoring CO_2 injection: a case study from the Ketzin Site, Germany. *Geophysical Journal International* **189**, 629-646.

Table 1 Template acquisition parameters for the first post-injection survey.

Parameter	Value
Receiver line spacing/number per template	96m/5
Receiver station spacing/channels per template	24m/48
Source line spacing/number per template	48m/12
Source point spacing	24m or 72m
CDP bin size	12m × 12m
Nominal fold	25
Geophones	28 Hz single
Sampling rate	1 ms
Record length	3s
Source	240 kg accel. weight drop, 8 hits per shot point
Acquisition unit	Sercel 428 XL

Table 2 Processing steps applied to the first post-injection 3D dataset.

Step	Processing workflow and parameters
1	Read raw SEGD data
2	Vertical diversity stack
3	Bulk static shift (correction for instrument delay)
4	Extract and apply geometry
5	Trace editing
6	Notch filter: 50 Hz
7	Spherical divergence correction
8	Band-pass filter: 7-14-120-200 Hz
9	Surface consistent deconvolution: 120 ms, gap 16 ms, white noise 0.1%
10	Ground roll mute
11	Spectral equalization: 20–35–80–110 Hz
12	Band-pass filter: 0–300 ms: 15–30–75–115 Hz; 350–570 ms: 14–28–70–110 Hz; 620–1000 ms: 12–25–60–95 Hz
13	Zero-phase filter: converts an average near minimum-phase wavelet of the weight drop source to a wavelet being closer to zero phase
14	Time-lapse difference static correction (with reference to baseline survey)
15	Trace balance using data window
16	NMO
17	Residual statics
18	Stack
19	Trace balance
20	FX-Decon: inline and crossline directions
21	Trace balance
22	Migration: 3D FD using smoothed stacking velocities

Table 3 CO_2 mass calculated from simulations.

	Total CO_2 mass (kt)	Gaseous CO_2 mass (kt)	CO_2 thickness threshold (m)	Percentage (%) of gaseous CO_2 mass when thickness <= threshold	Gaseous CO_2 mass (kt) when thickness > threshold
2009	22	15.8	5 (Lüth et al. 2015)	29.4	11.2
2012	61	43.9	6 (Lüth et al. 2015)	44.4	24.4
2015	67	45.2	6	47.93	23.6
			7	62.9	16.8

Table 4 Average CO_2 saturations from results of PNG logging for 3D seismic repeat two (PNG repeats R6, Ktzi 200/201, and R2, Ktzi 203) and three (PNG repeats R9, Ktzi 200, R8, Ktzi 201, and R5, Ktzi 203), and averaging interval parameters (see Fig. 12 and text for further details).

Well	Interval Nr.	Top	Bottom	Thick-ness	Phi	3D repeat two		3D repeat three
						Sg min.	Sg max.	Sg
		(m)	(m)	(m)	(%)	(%)	(%)	(%)
201	1	633.75	642.09	8.34	23.5	50	56	44
	2	642.87	650.99	8.12	25.9	15	21	-
	3	657.89	661.85	3.96	26.3	-	-	19
	4	661.85	664.11	2.26	27.2	-	-	1
	Eff.					33	39	31
200	1	634.58	642.24	7.66	27.5	58	58	36
	2	643.66	649.49	5.83	29.6	-	-	-
	Eff.					58	58	36
203	1	631.12	639.17	8.05	25.9	80	80	64

Table 5 Respective parameter choices for the three repeat surveys.

	Conversion of normalized 4D amplitude (ΔA) to CO_2 saturation (S_{CO2})	Density of CO_2 (kg/m3)	Porosity (%)	Normalized 4D amplitude threshold	Time shift threshold	Calculated mass (kt)
Repeat 1 (Ivanova *et al.* 2012)	$S_{CO_2}(\Delta A) = \begin{cases} 33\%, \Delta A<0.4 \\ 42\%, 0,4<\Delta A<0.6 \\ 48\%, \Delta A>0,6 \end{cases}$	266.62	20	0.3	1.5 ms	23.83
Repeat 2 (Ivandic *et al.* 2015)	$S_{CO_2}(\Delta A) = 50\%$	215	20	0.3	1.5 ms	52.51
Repeat 1 (this study)	$S_{CO_2}(\Delta A) = \begin{cases} 33\%, \Delta A<0.4 \\ 42\%, 0,4<\Delta A<0.6 \\ 48\%, \Delta A>0,6 \end{cases}$	266.62	20	0.3	1.5 ms	26.84
Repeat 2 (this study)	$S_{CO_2}(\Delta A) = \begin{cases} 33\%, \Delta A<0.4 \\ 42\%, 0,4<\Delta A<0.6 \\ 48\%, \Delta A>0,6 \end{cases}$	215	20	0.3	1.5 ms	55.66
Repeat 3 (this study)	$S_{CO_2}(\Delta A) = \begin{cases} 33\%, \Delta A<0.4 \\ 42\%, 0,4<\Delta A<0.6 \\ 48\%, \Delta A>0,6 \end{cases}$	184.2	20	0.3	1.5 ms	10.80
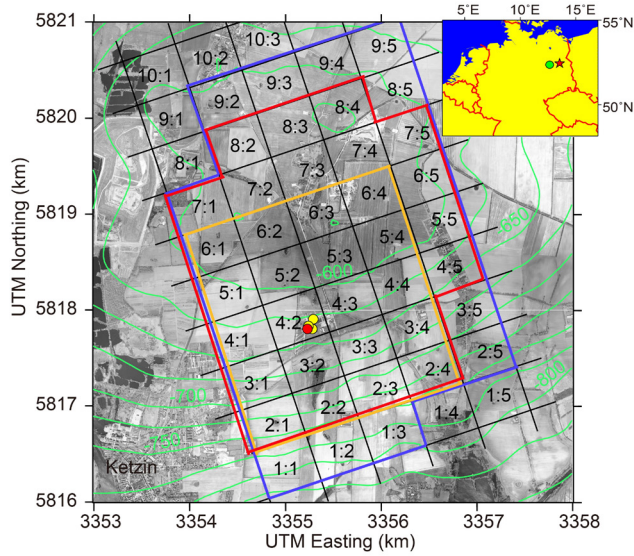
Figure 1 Template schemes used in the previous 3D surveys. Blue, orange and red polygons indicate the areas of the baseline, first repeat and second repeat surveys, respectively. Red and yellow dots show the locations of the injection well (Ktzi 201) and three observation wells (Ktzi 200, 202, and 203), respectively. Topography of the storage formation is marked by the green isolines. Inset shows the location of Ketzin (green dot), west of Berlin (red star), Germany.
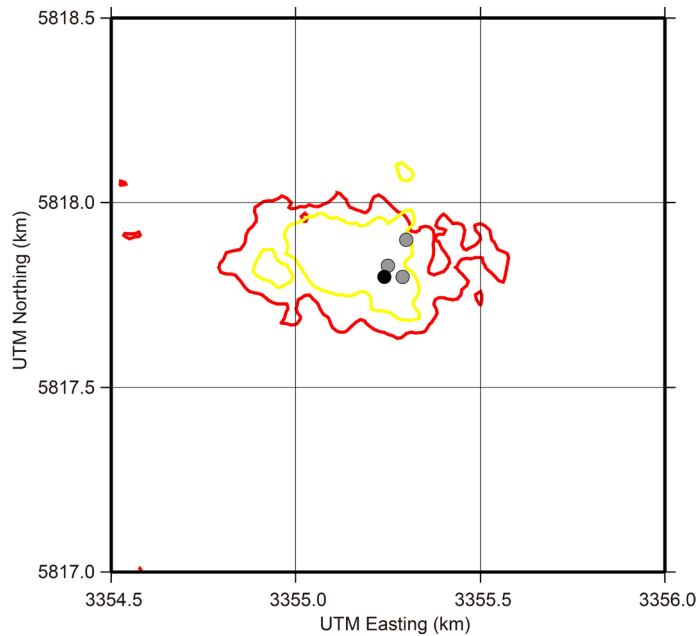

Figure 2 Contour lines at the 0.3 level extracted from the amplitude difference (baseline minus repeat) horizons at the reservoir top level. The amplitude was normalized to the K2 peak amplitude. Yellow and red lines represent the outlines of the CO_2 plume for the first and second repeat surveys, respectively. Black and gray dots indicate the locations of the injection well and three observation wells, respectively.
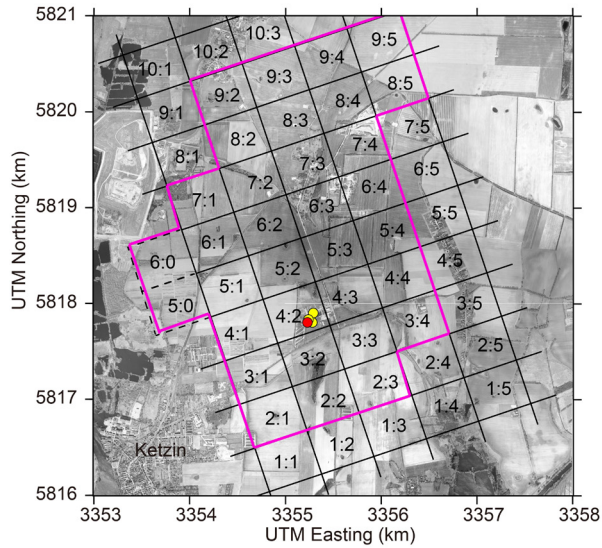
Figure 3 Template schemes used in the first post-injection 3D survey. Magenta polygon indicates the first post-injection survey area. Red and yellow dots show the locations of the injection well and three observation wells, respectively.
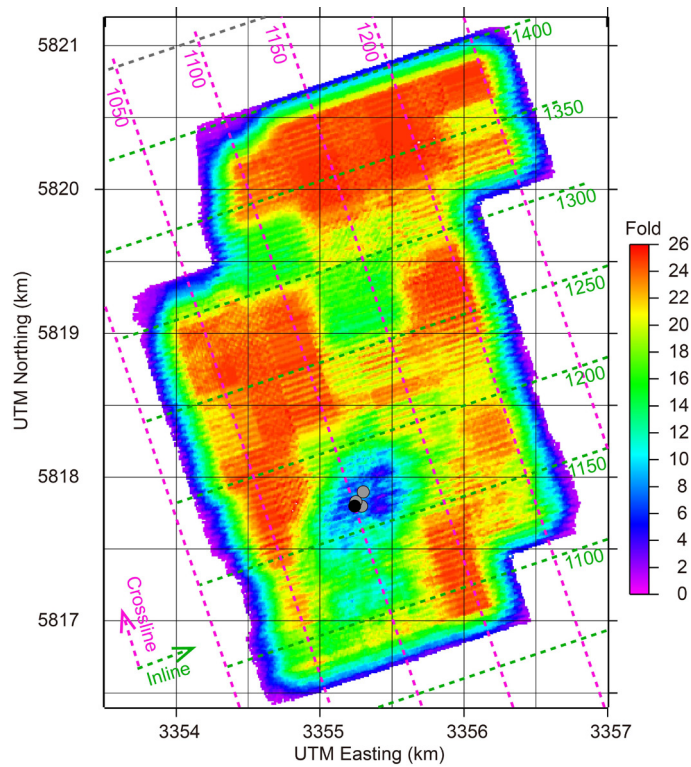
Figure 4 Actual CDP fold of the first post-injection survey with inlines (green dashed lines) and crosslines (magenta dashed lines). Black and gray dots indicate the locations of the injection well and three observation wells, respectively.
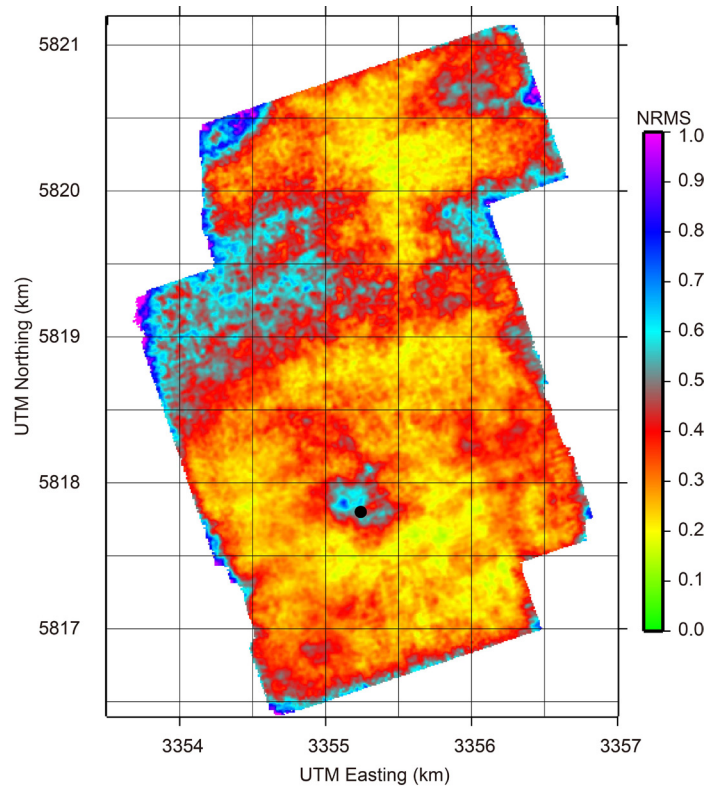
Figure 5 Map of the NRMS deviation between the baseline and first post-injection subvolumes after cross-equalization in the 100-700 ms time window. Black dot indicates the location of the injection well.
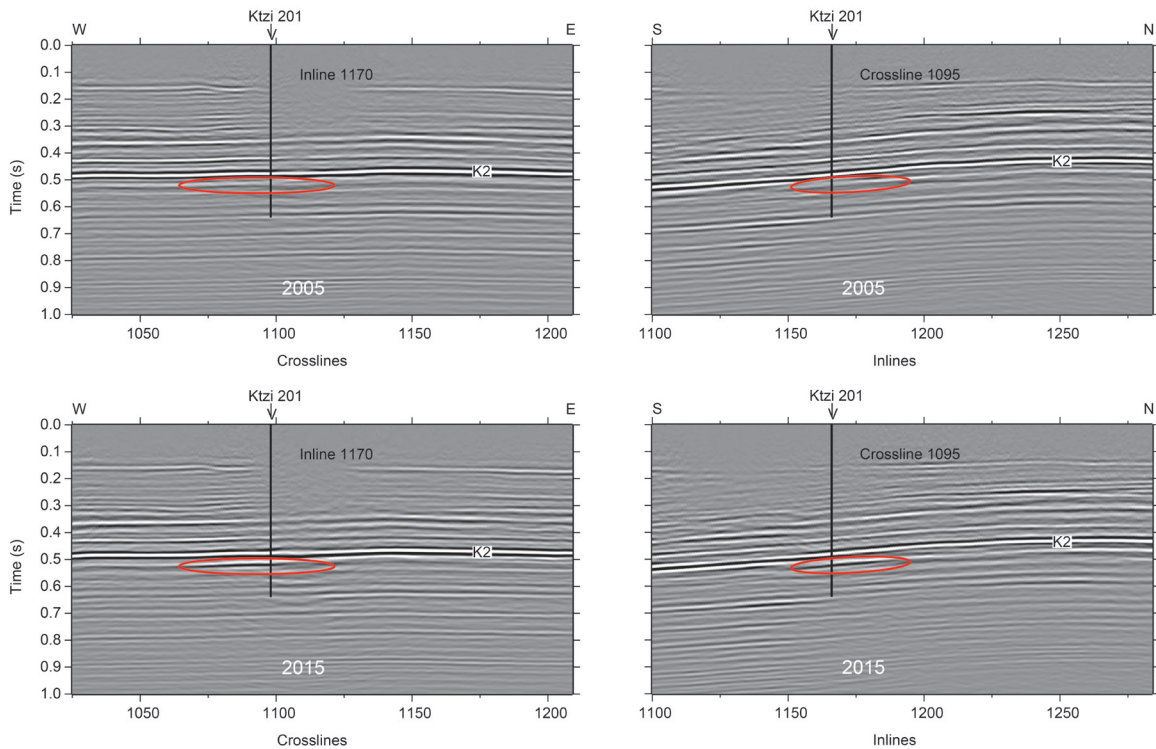
Figure 6 Time-migrated sections along inline 1170 (left panel) and crossline 1095 (right panel). From top to bottom: baseline and first post-injection subvolumes. The target area is highlighted by red ellipses. The first post-injection sections show stronger seismic responses caused by the injected CO_2. The location of the injection well is marked by the black vertical line.
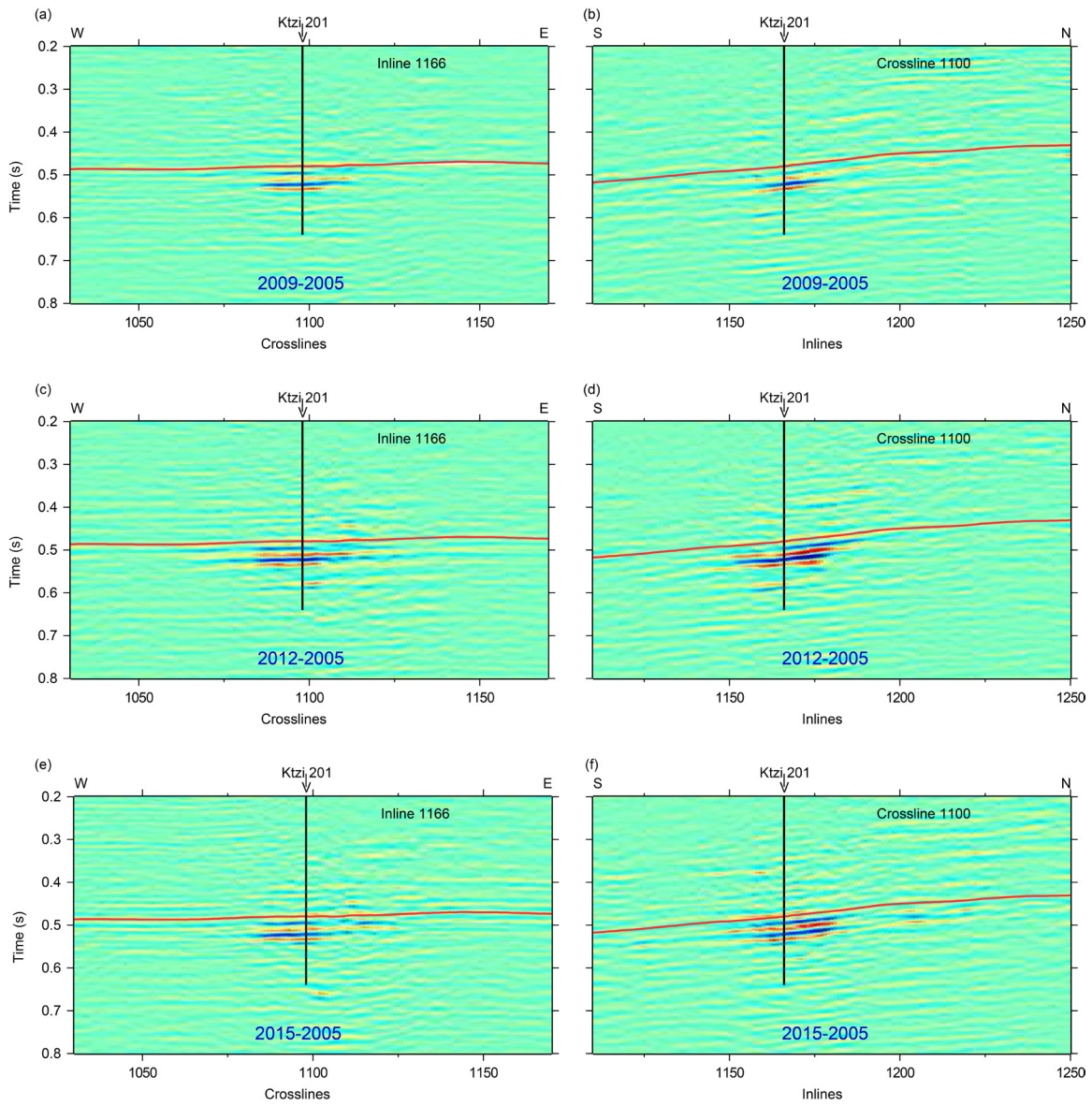
Figure 7 Vertical sections of time-lapse amplitude difference (repeat minus baseline) along inline 1166 (left panel) and crossline 1100 (right panel). From top to bottom: first repeat, second repeat and first post-injection results. The red line represents the K2 horizon. The location of the injection well is marked by the black vertical line.
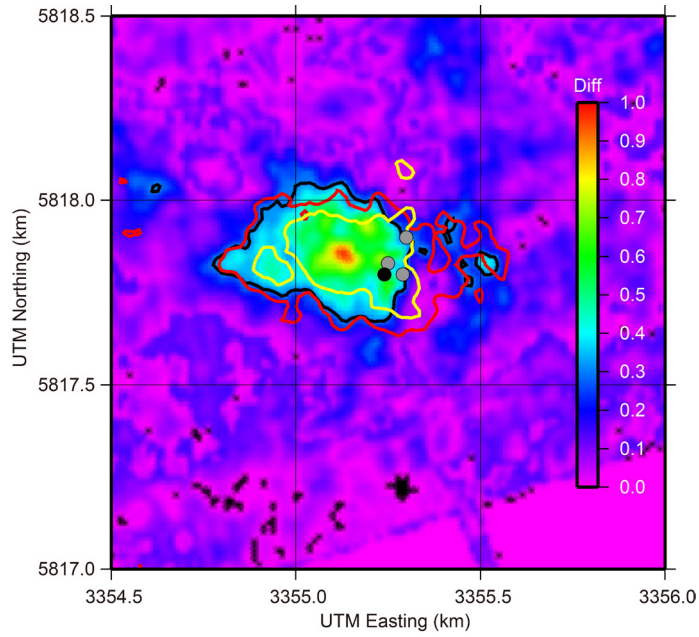
Figure 8 Normalized amplitude difference (baseline minus repeat) map at the reservoir level for the first post-injection survey. Yellow, red and black contour lines at the 0.3 level represent the outlines of the imaged CO_2 plume for the first repeat, second repeat and first post-injection surveys, respectively. Black and gray dots indicate the locations of the injection well and three observation wells, respectively.
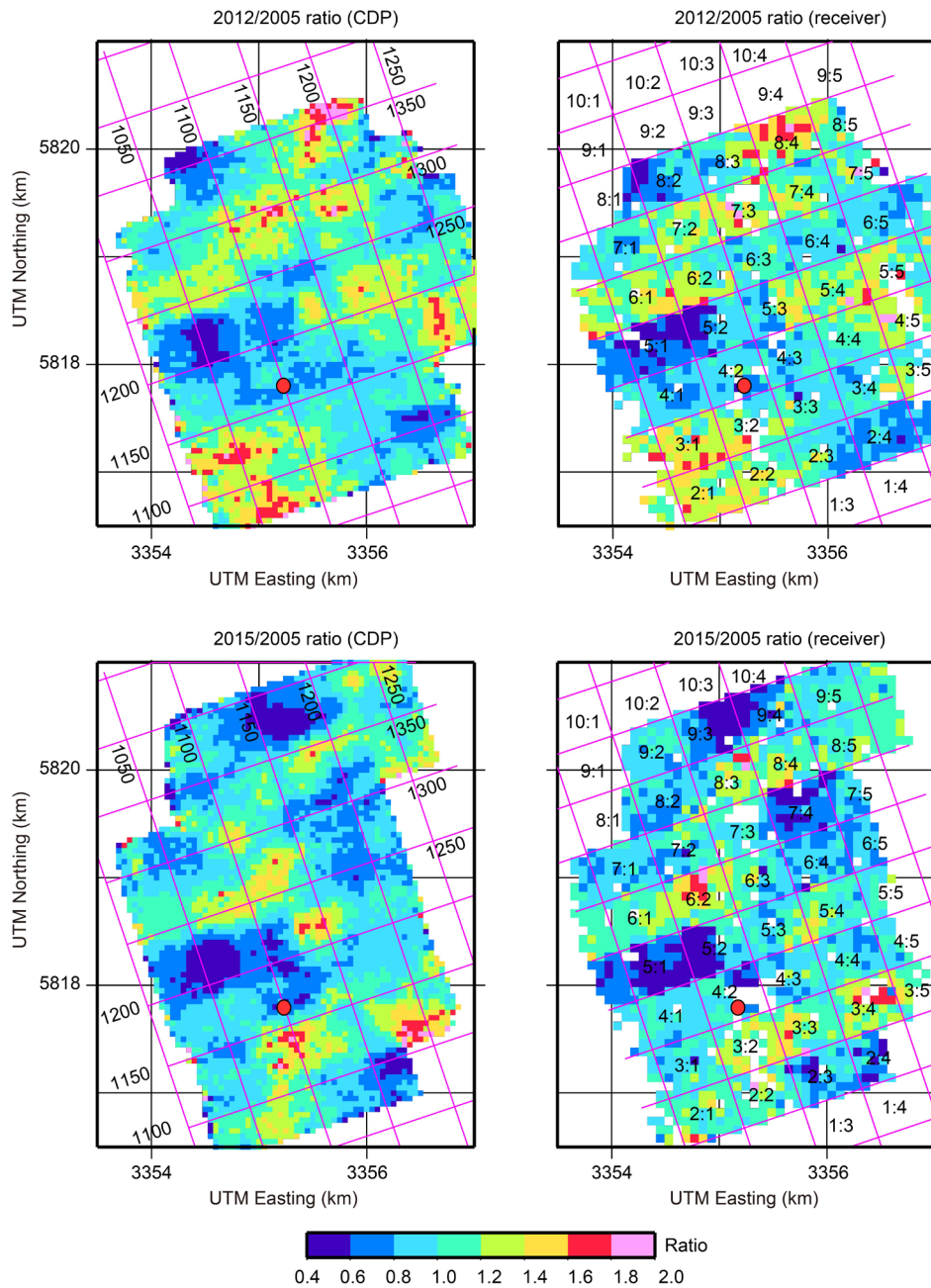
Figure 9 Maps of the ratio of signal-to-noise ratio as a function of CDP location (left panel) with inlines and crosslines and receiver location (right panel) with template system. From top to bottom: 2012/2005 ratio and 2015/2005 ratio. Red dot indicates the location of the injection well.
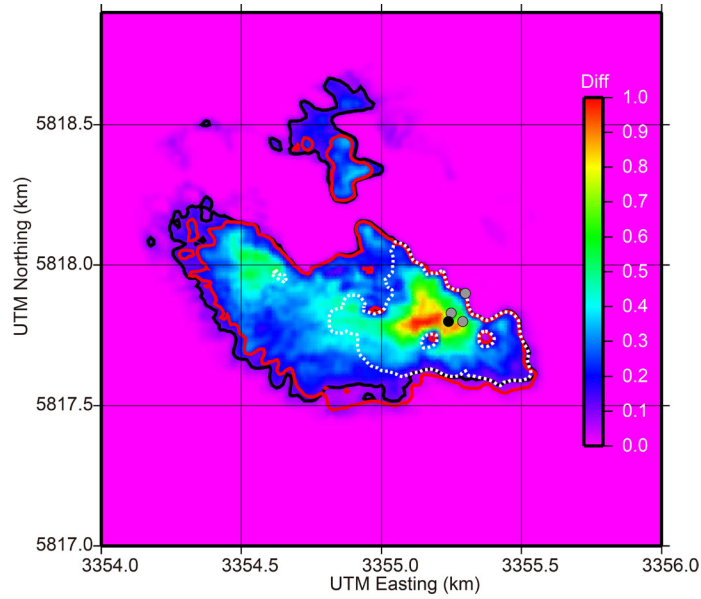
Figure 10 Normalized amplitude difference (baseline minus repeat) map at the reservoir level from the synthetic first post-injection dataset. The outline of the amplitude anomaly (contour lines at the 0.1 level) is marked by a black solid line. White dashed line represents the outline of the amplitude with the CO_2 thickness threshold of 7 m. Red solid line (contour lines at the 0.1 level) highlights the outline of the amplitude anomaly at the second repeat time. Black and gray dots indicate the locations of the injection well and three observation wells, respectively.
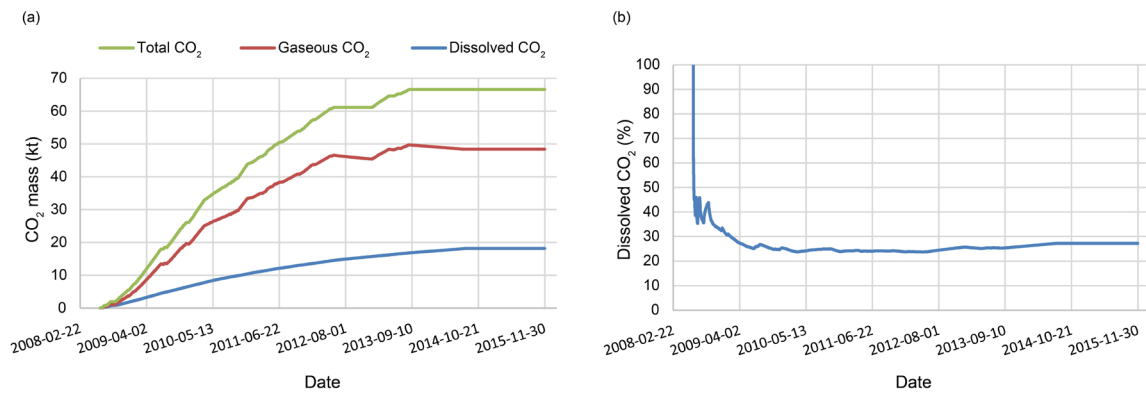
Figure 11 (a) CO_2 mass balance and (b) CO_2 dissolution ratio obtained from the reservoir simulations. Green, red and blue lines show CO_2 mass of total injected CO_2, gaseous CO_2 and dissolved CO_2, respectively.
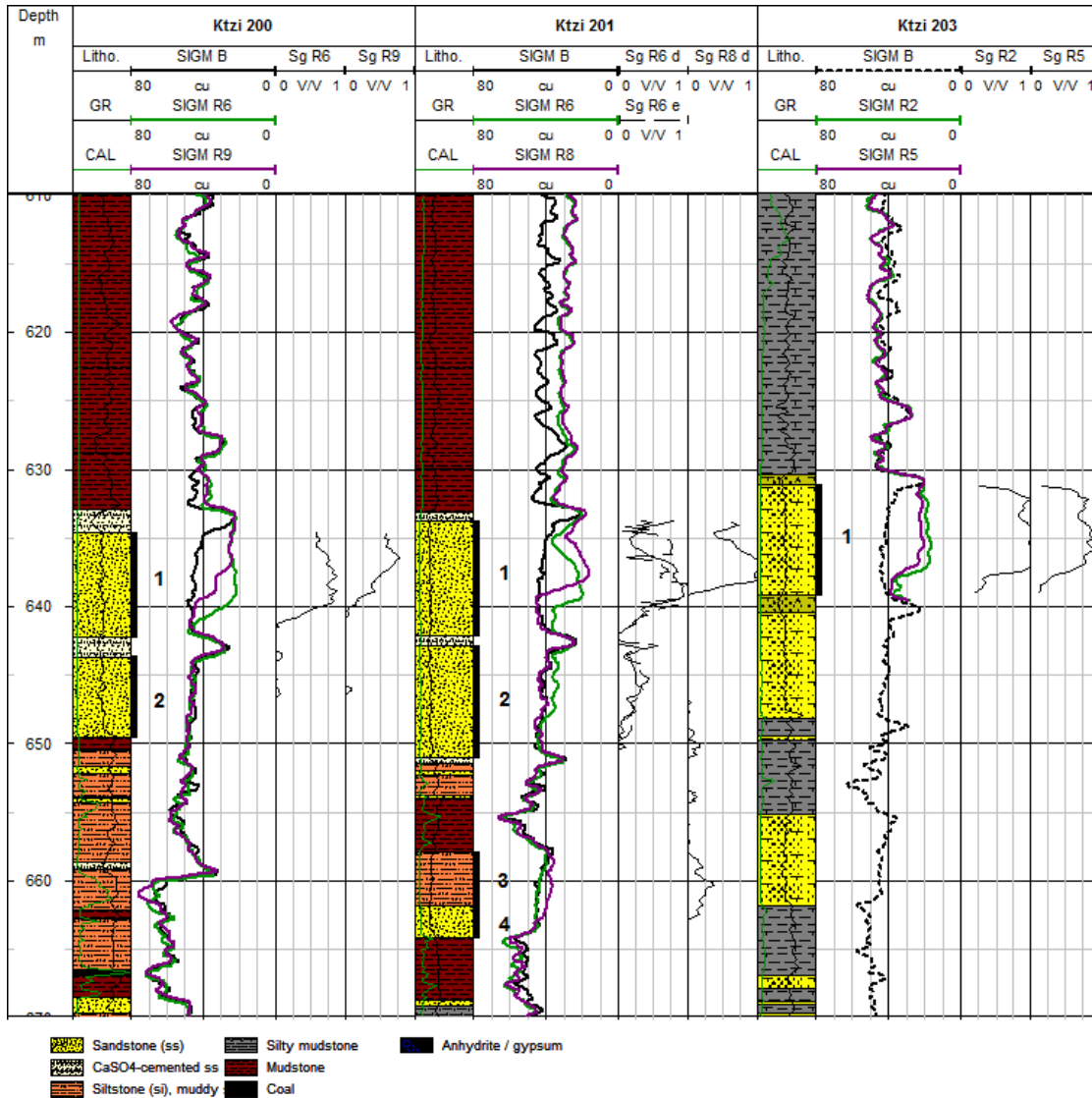
Figure 12 Measured PNG Σ formation (SIGM) log curves of the baseline (B) and repeat (R) logging runs closest to the second (green) and first post-injection (purple) 3D seismic repeats (dates of individual runs are listed within the text), as well as calculated CO_2 saturations (Sg, d: displacement, e: extended PNG saturation models). Numbers of depth intervals for calculation of average CO_2 volumes and saturations (see Table 4) are indicated with black bars and bold numerals. Lithology after (Förster *et al.* 2010).
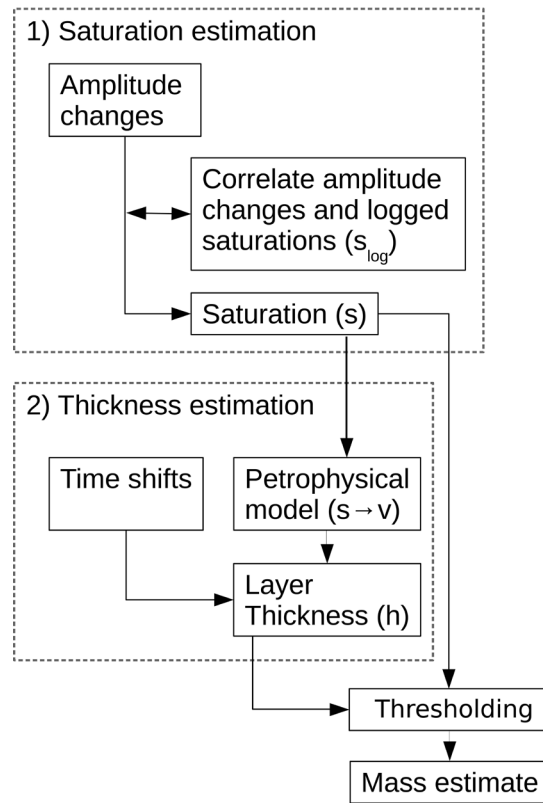
Figure 13 The workflow used by Ivanova *et al.* (2012) and Ivandic *et al.* (2015) for CO_2 mass estimations at Ketzin (3D seismic repeat surveys of 2009 and 2012).
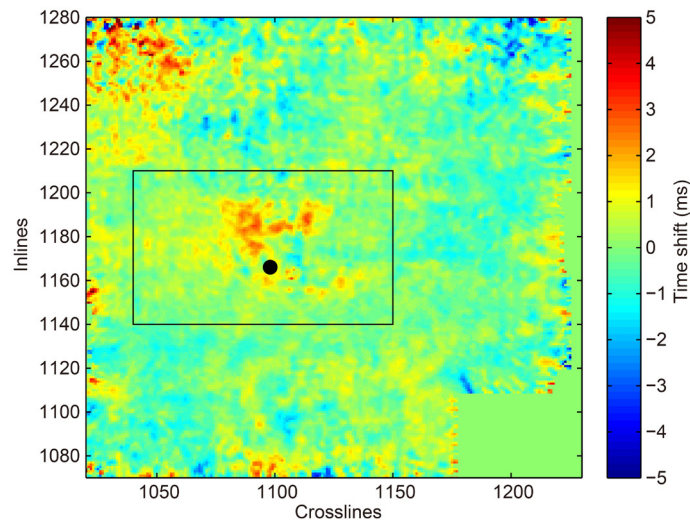
Figure 14 Time-delays obtained from differences between the time shifts of the windows above and below the reservoir (between baseline and 2015 repeat survey). The location of the injection well is marked with the black dot. The area used for CO_2 mass quantifications is marked by the black frame.
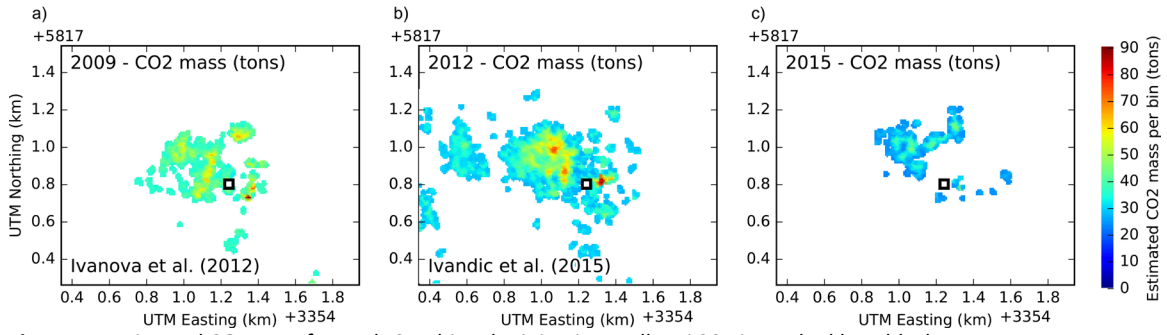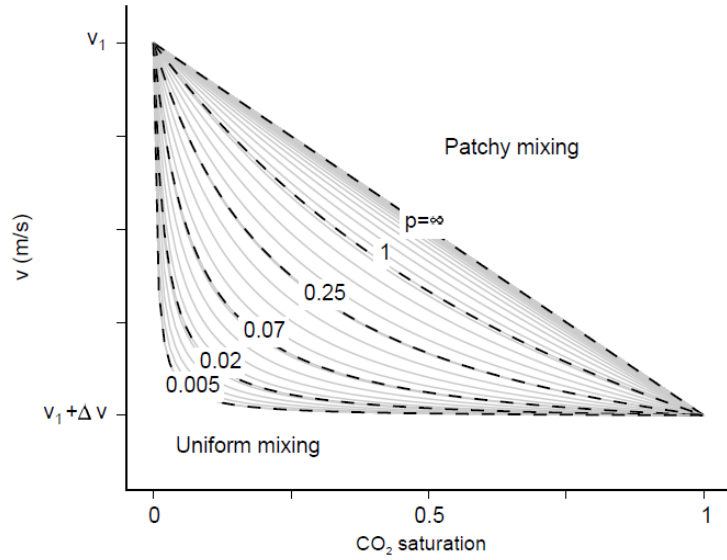
Figure 15 Estimated CO_2 mass for each CDP bin. The injection well Ktzi 201 is marked by a black square.
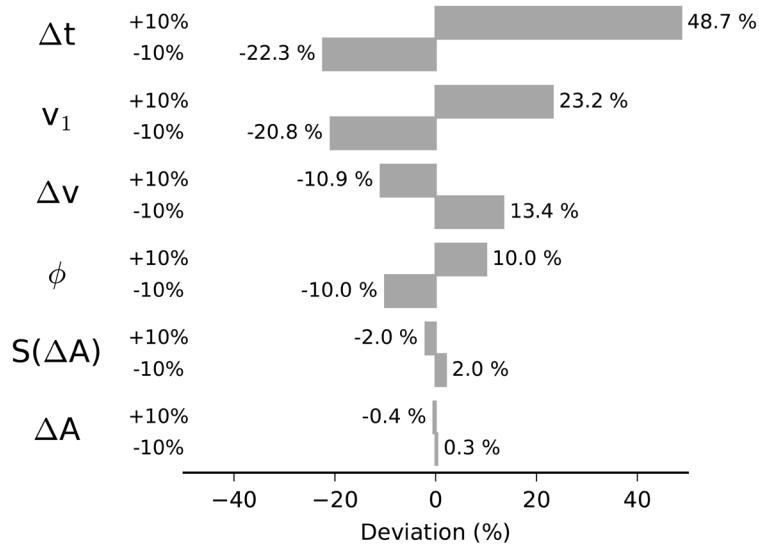

Figure 16 The impact of uncertain reservoir parameters in the calculated CO_2 mass in 2015.
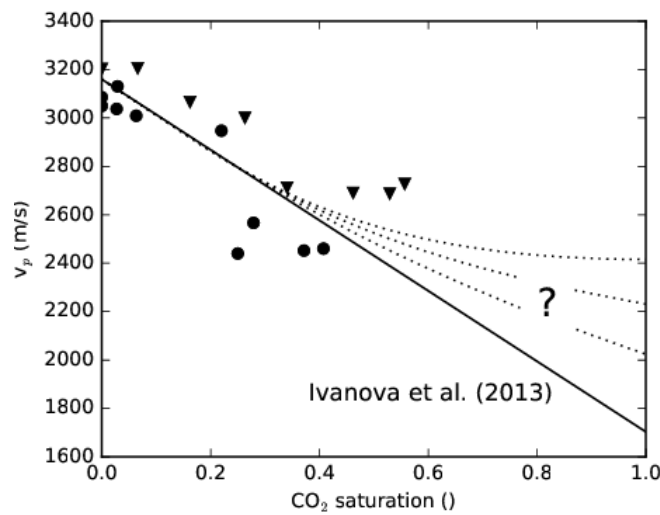

Figure 17 Compressional wave velocity, v_p, for variable CO_2 saturation inferred for two core samples from Ketzin after Ivanova *et al.* (2013b). The solid line shows the velocity-saturation relationship presented by Ivanova *et al.* (2013b).
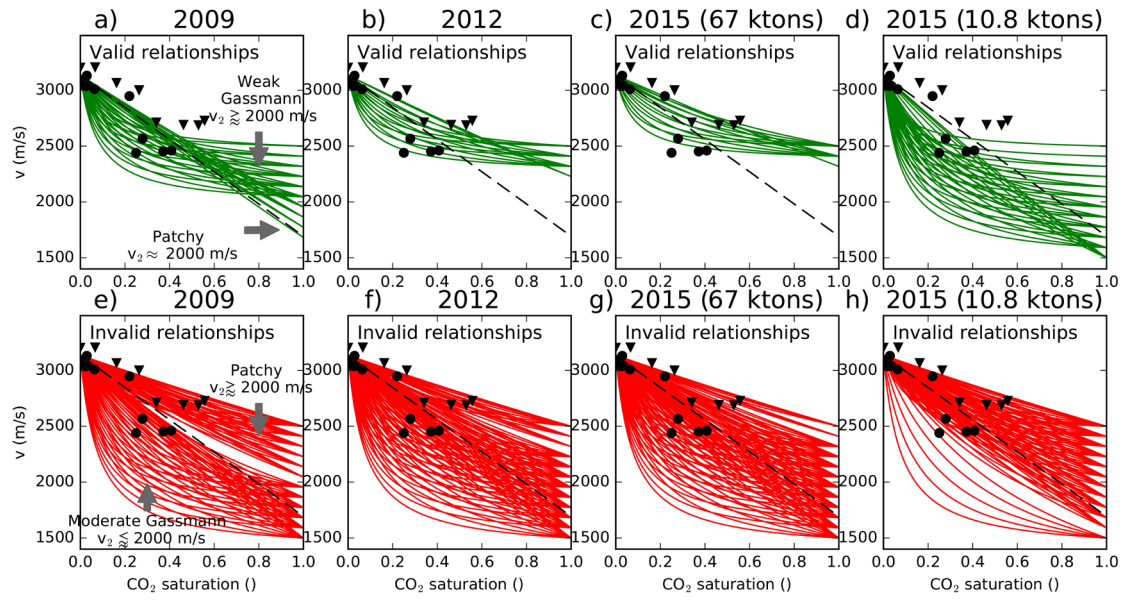
Figure 18 Set of velocity-saturation relationships computed from equation 6 using a variable patchiness parameter (marked graphs). Figure modified after Bergmann and Chadwick (2015).
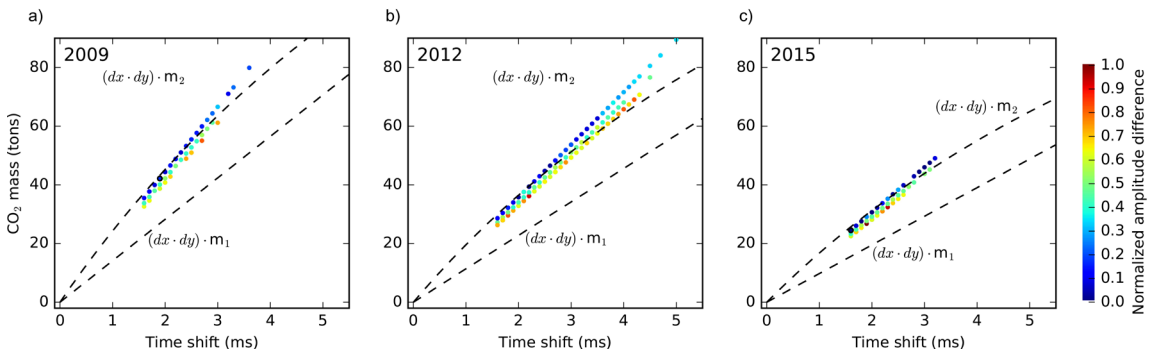
Figure 19 4D time shift and estimated CO_2 mass for each CDP bin. Black curves show bounds on the CO_2 mass per CDP bin, $(dx \cdot dy) \cdot m_1$ and $(dx \cdot dy) \cdot m_2$, derived from the time-shift approach.
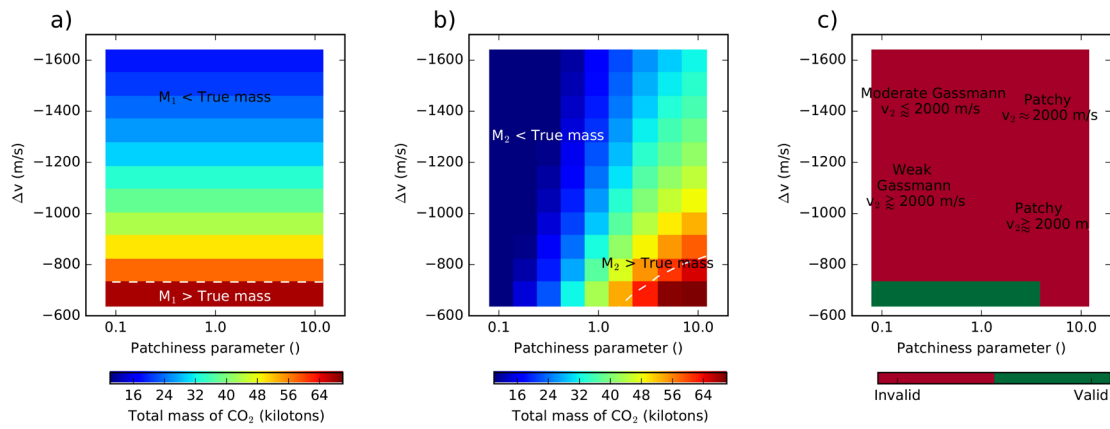
Figure 20 (a)-(b) Total CO_2 mass bounds, M1 and M2, for a range of patchiness parameters and velocity changes, Δv. (c) Comparison of the total CO_2 mass bounds with the true CO_2 mass (from 2015). Green indicates those scenarios where the mass bounds are consistent with the true mass. Red indicates the scenarios where the true mass lies outside the mass bounds.

Figure 21 Velocity-saturation relationships that are consistent (top row) and inconsistent (bottom row) with the CO_2 true mass injected at the times of the three repeat surveys.